Surface climate signals transmitted rapidly to deep North Atlantic throughout last millennium

Wanyi Lu[1]*, Delia W. Oppo[1], Geoffrey Gebbie[1], David J. R. Thornalley [1,2]

[1] Woods Hole Oceanographic Institution, Woods Hole, MA, USA

[2] Department of Geography, University College London, London, UK

*Corresponding author. Email: wlu@whoi.edu

Abstract:

Instrumental observations of subsurface ocean warming imply that ocean heat uptake has slowed 20th-century surface warming. We present high-resolution records from subpolar North Atlantic sediments that are consistent with instrumental observations of surface and deep warming/freshening and, in addition, reconstruct the surface-deep relation of the last 1,200 years. Sites from ~1300 meters and deeper suggest an ~ 0.5°C cooling across the Medieval Climate Anomaly to Little Ice Age transition that began ~1350 ± 50 Common Era (CE), whereas surface records suggest asynchronous cooling onset spanning ~ 600 years. These data suggest that ocean circulation integrates surface variability that is transmitted rapidly to depth by the Atlantic Meridional Ocean Circulation, implying that the ocean moderated Earth's surface temperature throughout the last millennium as it does today.

One-Sentence Summary:

Surface climate changes of the last 1,200 years were transferred rapidly to the deep North Atlantic.

Main Text:

Earth's surface has generally warmed over the last century (*1*), but the ocean has slowed this warming by taking up over 90% of the excess thermal energy since 1955 (*2*) and increasingly storing it in the deep oceans (*3–5*). Climate reconstructions provide a baseline for assessing the anomalous nature of twentieth century change and the role of the deep ocean in moderating surface climate on longer time scales. The Common Era (i.e., the last ~2,000 years, CE) contained significant climate variability, including a cooling trend from the peak of the Medieval Climate Anomaly (MCA, around 850-1250 CE) to the Little Ice Age (LIA, around 1400-1850 CE), and rapid industrial warming since ~1850 (*1*, *6*). The high-latitude North Atlantic Ocean is an important region where deep water forms and surface temperature anomalies are expected to be transported efficiently to depth via the Atlantic Meridional Overturning Circulation (AMOC) (*7*). However, few high-resolution records from the deep North Atlantic span the MCA-LIA transition (*8*), and the hypothesis that an active AMOC moderated surface climate on centennial time scales across this transition has not been evaluated with deep North Atlantic proxy records. Here we present data from well-dated sediment cores that form a depth transect spanning ~1000-2300 m and sample several important water masses in the subpolar North Atlantic. These data permit us to compare changes in the properties of the Nordic Overflows to those of waters formed south of the Nordic Seas, and with the insights of a model, place aspects of modern ocean warming in a longer-term context.

We used 11 marine sediment cores from south of Iceland along the eastern flank of Reykjanes Ridge, collected in 2014 on the research vessel R/V Endeavor (cruise EN539) (Table S1, Fig. 1). Iceland Scotland Overflow (ISOW) entering the northern Iceland Basin is much denser than the ambient Atlantic intermediate waters near the sill depths (~500 – 800 m), resulting in vigorous mixing and entrainment, especially during its initial descent, but also as it flows along the flank of the Reykjanes Ridge (*9*). A water mass decomposition from an inversion of oceanographic data (Fig. S1-S2, (*10*)) indicates that all our core sites contain a mixture of ISOW, colder, fresher Labrador Sea Water (LSW), and warmer, saltier Subpolar Mode Water (SPMW). SPMW is most prevalent at the shallowest site, whereas the ISOW contribution increases with depth, reaching a maximum of nearly 60% at our deepest site. The LSW contribution is relatively constant with depth, with a maximum at about 1300 m. Higher seawater density north of the sills compared to south of them has largely driven the transport of overflow waters over the last century (*11*).

We measured the oxygen and carbon isotope ratios, $\delta^{18}O$ and $\delta^{13}C$ (the $^{18}O/^{16}O$ and $^{13}C/^{12}C$ in each sample, relative to that of an international standard), in two species of planktic foraminifera (*Globigerina bulloides*, which calcifies in the upper ~50 m (*12*), and *Globorotalia inflata*, which calcifies as deep as ~300 m (*13*)), and in one of two species of benthic foraminifera (*Cibicidoides wuellerstorfi* or *Uvigerina peregrina*), depending on their availability. Variations in the $\delta^{18}O$ of foraminifera reflect variations in calcification temperature and the $\delta^{18}O$ of seawater, the latter in turn influenced by salinity (*14*); foraminiferal $\delta^{18}O$ increases with increasing seawater $\delta^{18}O$ and with decreasing temperature. In addition, *C. wuellerstorfi* calcifies in equilibrium with seawater, but $\delta^{18}O$ values in *U. peregrina* are ~0.47 ‰ higher (*14*). In the modern subpolar North Atlantic below 1000 m (*15*), variations in the $\delta^{18}O$ of calcite are largely due to temperature variability ($R^2 = 0.93$) rather than salinity ($R^2 = 0.00$) (Fig. S3), and modern measured benthic $\delta^{18}O$ closely follows the predicted $\delta^{18}O$ of calcite (Fig. S2). Chronologies and their uncertainties were constrained by radiocarbon data and determined using Bayesian methods (*16*) (Methods). All cores have high sediment accumulation rates (~ 25 – 70 cm/1000 years) and, except for MC22A and MC13A, have modern core tops as indicated by radiocarbon (fraction

modern (Fm) >1) (Table S1, Fig. S4). The records span the last ~500 – 2,250 years (Fig. 2, Data S1-3, Fig. S5-14).

Rapid Transmission of Common Era Surface Climate Trends to Depth

All but one planktic $\delta^{13}C$ records from cores with Fm >1 show a sharp decrease in recently-deposited sediments (Fig. S9, S11, S12), reflecting the oceanic uptake of isotopically light anthropogenic carbon released by fossil fuel burning since the early 19th century (*17*). The rapid decrease of planktic $\delta^{13}C$ near the top of MC13A suggests its top is modern despite its relatively low Fm value. Eight out of the 10 benthic records from cores with modern tops have lowest values near their tops. Of these, the $\delta^{13}C$ decrease is significant relative to the post-1850 period in six records (Fig. S7, S12). The amplitude of the $\delta^{13}C$ decrease in the benthic records ranges from about 0.1 to 0.4 ‰, consistent with modelled amplitude (*18*). The finding of low core-top $\delta^{13}C$ in the benthic records confirms an important role for AMOC in sequestering anthropogenic carbon into the deep ocean.

Most planktic $\delta^{18}O$ records from cores with modern tops show a decrease since the early 20th century, suggesting warming and/or freshening (Fig. 2, S8, S10). At least half of the benthic $\delta^{18}O$ records also show a decrease during this time period (Fig. 2, S6), although the signals are smaller than in the planktic records, and a statistical test, discussed below, was used to establish their significance. Most benthic and planktic records extending into the MCA appear to show a $\delta^{18}O$ increase across the MCA-LIA transition, suggesting cooling and/or increasing salinity. However, at the shallowest site (MC28A, ~1000 m) the benthic $\delta^{18}O$ decreases across the MCA-LIA transition and through most of the LIA. The amplitude of the MCA-LIA benthic $\delta^{18}O$ increase is also relatively small at the next deepest site (MC26A, ~1200 m) compared to the deeper sites.

To determine whether and when significant changes in the mean of $\delta^{18}O$ time series occurred, we computed the change points of the $\delta^{18}O$ records, adapting a method that accounts for age uncertainty and data variability and was previously used to detect AMOC strength change (*19*) (Methods). We divided the $\delta^{18}O$ records into post-1850 and pre-1850 datasets, and conducted change point analyses on each time interval. For the post-1850 interval, we excluded MC22A, which does not have a modern core top. For the pre-1850 dataset, we only included the six cores with Bayesian ensemble median ages older than 1200 CE (Table S1). For each core and foraminifera species, we computed the average $\delta^{18}O$ difference before and after the change point if the significance test was passed (Fig. 3). Key findings from these change point analyses are: (1) most planktic (15 out of 20) and half of the benthic (5 out of 10) records show statistically significant 20th century $\delta^{18}O$ decreases; (2) most planktic (10 out of 15) and benthic (5 out of 6) records show statistically significant $\delta^{18}O$ increases across the MCA-LIA transition; and (3) of the records with a significant $\delta^{18}O$ increase across the MCA-LIA transition, the average ages of the benthic $\delta^{18}O$ change points are in a narrow range, ~1346 ± 49 CE, whereas the planktic $\delta^{18}O$ change points occur across an ~600-year range, between 1100 and 1700 CE (average ~1357 ± 216 CE) (Data S4). The large range of planktic change points may reflect earlier cooling at our northern than southern sites (Fig. S15). Bioturbation, coupled with higher abundances of the planktic foraminifera near the tops of the cores, may have resulted in a small (~ 2-3 cm) downcore shift of the recent planktic $\delta^{18}O$ decrease (Figs. S16-17), implying that the post-1850 change point may have been more recent than implied by our analyses. Composites of raw $\delta^{18}O$ data from all cores on their median Bayesian ages confirm larger variability in the planktic $\delta^{18}O$ than benthic $\delta^{18}O$ records (Fig. S14).

We interpret the 20th-century $\delta^{18}O$ decrease recorded in the planktic records as rapid warming and freshening of subpolar surface and near-surface North Atlantic waters, consistent with planktic faunal changes in the same cores ((*20*), Fig. S18) and instrumental evidence indicating surface or near-surface warming and freshening trends since the 1950s both basin-wide (*21*, *22*) and locally (*23*) (Fig. S19). The smaller magnitude of the benthic (0.04 - 0.22 ‰) than planktic $\delta^{18}O$ decreases (0.06 - 0.43 ‰) in the late 20th century (Fig. 3B) is consistent with a recent, rapid, high-amplitude surface signal that was diluted by mixing with older waters in transit to the deep core sites. Thus, the corresponding trends of decreasing $\delta^{18}O$ and direct observations of recent warming and freshening imply that we can use the $\delta^{18}O$ signals in these cores to infer past changes related to seawater density.

With the exception of the MC25A *G. inflata* record, average planktic $\delta^{18}O$ was ~0.05 to 0.25 ‰ higher after the MCA-LIA change point than before it (Fig. 3A). At sites deeper than 1300 m, the mean benthic $\delta^{18}O$ is 0.05 to 0.14 ‰ higher after the MCA-LIA change point than before it. If these changes were driven by temperature, the benthic $\delta^{18}O$ increases would correspond to 0.2 – 0.6 °C average cooling (*14*). The smoothed benthic composite record suggests that on average, the deep sites (> 1300 m) increased by ~ 0.1‰, or cooled by ~ 0.5°C, similar to the change point results from individual records (Fig. 3A, S14). While temperature likely dominated the benthic $\delta^{18}O$ increases at these deep sites (> 1300 m), we cannot rule out that the $\delta^{18}O$ of one or more water masses influencing these sites changed across this transition.

Rapid transfer of surface signals to our deep core sites is consistent with young water mass ages at the sites (~35-65 years; Fig. S2) implied by a global inversion of modern oceanographic data (*10*). We infer that the greater range in the timing of change points in the planktic records across the MCA-LIA transition (1076 – 1712 CE), compared to the benthic records (1275 – 1395 CE) (Fig. 3A), is due to several factors, including larger seasonal and depth-habitat variations of planktic foraminifera, the time-transgressive nature of surface change, larger temporal variability in the surface (for example the meandering of zonal fronts on seasonal-interannual-decadal timescales), and a potential contribution due to bioturbation coupled with planktic foraminifera abundance changes (Supplementary text). Furthermore, the narrower range of benthic than planktic change points is the expected consequence of interior ocean mixing that damps surface variability. Globally-averaged temperature anomalies, for example, exhibit their greatest interannual variability above 500 m depth, but the deeper ocean is more representative of the longer-term ocean heat gain (*24*). Thus, the benthic records integrate the surface variability and more reliably record the overall timing of the MCA-LIA cooling/salinification.

Arctic Amplification of MCA-LIA Cooling

We compare our $\delta^{18}O$ records with results from an ocean model inversion (*25*) (referred to as OPT-0015 hereinafter), which fits an empirical ocean circulation model to modern-day tracer observations, historical deep-sea temperature in the 1870s (*26*), and global-mean Ocean2k sea surface temperature (SST) reconstructed for the Common Era (*6*) (Supplementary text). The OPT-0015 inversion solves for the three-dimensional evolution of temperature throughout the Common Era under the assumption of a fixed, modern-day ocean circulation. In the inversion, SST is allowed to vary regionally in order to fit the subsurface constraints. We extracted the OPT-0015 model temperature simulated at the model grid nearest our cores and converted the temperature into $\delta^{18}O$ changes using empirical calibrations (*14*). The model exhibits temporal trends consistent with those in the foraminiferal $\delta^{18}O$ records of the surface and the deeper sites (Figs. 2, 4), showing both LIA cooling and 20th-century warming.

To compare data and model change points, we first obtained model variability by computing 100-year moving averages in the surface mixed layer and at 2000 m depth, and then performed change point analyses on the moving averages (Fig. S20). For both the surface and deep sites, the post-1850 change point in the model and data are within error, especially considering chronological uncertainty in our records (Fig. 3B). On the other hand, there is a large data-model change point mismatch in the timing of significant LIA cooling/salinification, with the model change points occurring ~350 years before the average benthic and planktic change points (Fig. 3A). This occurs because the model was constrained with the Ocean2k SSTs (*25*), which contain cooling before and during the MCA, and which the model then faithfully reproduces. In contrast, other independent estimates of the timing of the LIA from regions proximal to our study area yield ages that are more consistent with the change point derived from our benthic $\delta^{18}O$ records (~1346 ± 49 CE), such as an Arctic temperature reconstruction (*27*) (~1258 ± 2 CE) and Greenland ice cap growth records (*28*) (~1353 ± 9 CE).

The model inversion suggests that for multi-centennial variability in the pre-1850s, including the MCA-LIA transition, temperature change in the deep sea (>1000 m) was greater than the upper ocean (< 500 m) (Fig. 4A). The smaller cooling in upper waters cannot be confirmed nor rejected with the planktic $\delta^{18}O$ records, as their signals may be complicated by several factors described above, however, the benthic $\delta^{18}O$ records in sites >1300 m are consistent with the model prediction of ~0.5 ºC LIA cooling in the deep sea (Fig. 3A). The reason that the deep sea cools more than the upper ocean during the simulated LIA is related to Arctic amplification of the LIA cooling, which is present in the SST inversion (*25*) and was also simulated in the Community Earth System Model-Last Millennium Ensemble (*29*). Thus, cooling in the Nordic Seas where the overflows originated was greater than in waters formed south of the sills (*25*, *29*). With an active AMOC, larger cold anomalies from the Nordic Seas are transmitted to depth via the overflows. Contrasting with the MCA-LIA cooling, modern warming is (thus far) concentrated in the upper ocean, both in observations and in OPT-0015 (Fig. 3B and 4B). During the MCA – LIA transition, the deep ocean had sufficient time to record the cooling which lasted ~ 600 years, whereas the time interval of 20th century warming was shorter. Thus, the core sites, having average water mass ages of 40-70 years (modern, Fig. S2), have not yet had sufficient time to fully record the warming at depth, and anomalies at depth will always lag those at the surface unless warming ceases.

MCA - LIA SPMW Freshening/Warming

The model inversion suggests a large cooling across the MCA-LIA transition that is not evident in the benthic $\delta^{18}O$ data of the two shallowest sites (MC28A and 26A) (Fig. 2). This benthic data-model mismatch likely reflects MCA-LIA oceanographic changes (i.e., changes in circulation, seawater $\delta^{18}O$, salinity), that were not considered in the inversion. The shallowest site, MC28A, which shows a trend of decreasing $\delta^{18}O$ from the MCA through the end of the LIA, is currently within the high salinity zone of SPMW (Fig. 1), which has been diluted by mixing with LSW and overflows (Figs. S1-2). It is possible that a cooling trend at site MC28A was compensated by freshening that is not considered in the model, and that the temperature-related $\delta^{18}O$ increase at MC26A was also dampened by freshening. Fresh, low-$\delta^{18}O$ polar waters may have been incorporated into SPMW, which most affects the two shallowest sites. This hypothesis is consistent with evidence of increased sea-ice export from the Arctic that began at ~1300 CE and continued through the LIA (*8*, *30*, *31*). SPMW freshening during the LIA was also inferred downstream of the eastern subtropical gyre (*32*). Alternatively, or in addition, a greater contribution of a fresher, lower-$\delta^{18}O$ upper LSW relative to SPMW to our shallow sites could

have resulted in the observed $\delta^{18}O$ decrease. Given that overflows entrain less dense waters during their descent along the ridge (*9*), it is possible that all our core sites were fresher during the LIA than MCA. If the LIA cooling from the OPT-0015 inversion (0.4 – 0.6 °C) is assumed accurate, cooling at all but one site would have been partially compensated by a decrease in $\delta^{18}O_{SW}$ (freshening) (Fig. S21). Such a freshening at depth may also explain why the benthic $\delta^{18}O$ data do not record the higher amplitude of the MCA-LIA deep cooling compared to the surface suggested by OPT-0015 (Figs. 3, 4, S20). However, we cannot rule out the possibility that the MCA-LIA trend of decreasing benthic $\delta^{18}O$ at our shallow site reflects warming of SPMW. Possible warming mechanisms include greater transport of warm subtropical waters to the SPMW formation regions (*33*, *34*) or a weakening AMOC, which results in upper ocean subsurface warming due to reduced convection and exchange with the overlying cold atmosphere (*35*).

Conclusion

Our data provide strong support for a persistent role of the AMOC in transferring anomalous upper ocean heat and freshwater to depth during the last ~1,200 years. The records indicate a deep ocean that cooled and lost heat during the LIA, implying that the heat was transferred to the upper ocean and atmosphere (*25*). Thus, the ocean acted to dampen MCA- LIA surface change much like it is dampening surface warming during the industrial era. Whereas modern warming is surface intensified, typically in the upper ~700 m (*2*), our model simulation suggests that on longer time scales, temperature change in the deep subpolar North Atlantic exceeds that in the upper ocean, consistent with polar amplification of temperature change and an active overflow. The model simulation we used assumes that the intensity of the AMOC was unchanged from the modern. If the AMOC has declined during the 20th century as several studies suggest (*36*, *37*), and AMOC during most of the Common Era was stronger, then the pre-20th-century AMOC may have played a larger role in transferring surface climate signals to depth than in the modern.

References and Notes

1. R. Neukom *et al.*, *Nat Geosci*. **12**, 643-649 (2019), doi:10.1038/s41561-019-0400-0.
2. S. Levitus et al., *Geophys. Res. Lett.* **39**, L10603 (2012). doi:10.1029/2012GL051106.
3. G. A. Meehl, J. M. Arblaster, J. T. Fasullo, A. Hu, K. E. Trenberth, *Nat. Clim. Chang.* **1**, 360–364 (2011). doi:10.1038/nclimate1229.
4. X. Chen, K. K. Tung, *Science* **345**, 897-903 (2014). doi:10.1126/science.1254937.
5. M.-J. Messias, H. Mercier, *Commun. Earth Environ*. **3**, 118 (2022). doi:10.1038/s43247-022-00443-4.
6. H. v. McGregor et al., *Nat. Geosci.* **8**, 671–677 (2015). doi:10.1038/ngeo2510.
7. B. Dickson et al., *Nature* **416**, 832-835 (2002). doi:10.1038/416832a.
8. P. Moffa-Sánchez et al., *Paleoceanogr. Paleoclimatol.* **34**, 1399-1436 (2019). doi:10.1029/2018PA003508.
9. H. R. Langehaug et al., *Paleoceanography*. **31**, 399–415 (2016). doi:10.1002/2015PA002920.
10. G. Gebbie, P. Huybers, *J Phys. Oceanogr.* **42**, 291-305 (2012). doi:10.1175/JPO-D-11-043.1.

11. T. Rossby, L. Chafik, L. Houpert, *Geophys. Res. Lett.* **47**, e2020GL087456 (2020). doi:10.1029/2020GL087456.

12. L. Jonkers, S. van Heuven, R. Zahn, F. J. C. Peeters, *Paleoceanography* **28**, 164-174 (2013). doi:10.1002/palo.20018.

13. A. Rebotim et al., *J. Micropalaeontol.* **38**, 113-131 (2019). doi:10.5194/jm-38-113-2019.

14. T. M. Marchitto et al., *Geochim. Cosmochim. Acta.* **130**, 1-11 (2014). doi:10.1016/j.gca.2013.12.034.

15. G. A. Schmidt, G. R. Bigg, E. J. Rohling, Global Seawater Oxygen-18 Database - v1.22 (1999). (available at https://data.giss.nasa.gov/o18data/)

16. N. P. McKay, J. Emile-Geay, D. Khider, *Geochronology* **3**, 149-169 (2021). doi:10.5194/gchron-3-149-2021.

17. C. D. Keeling, *Environ. Int.* **2**, 229-300 (1979). doi:10.1016/0160-4120(79)90005-9.

18. M. Eide, A. Olsen, U. S. Ninnemann, T. Eldevik, *Global Biogeochem. Cycles* **31**, 492-514 (2017). doi:10.1002/2016GB005472.

19. L. Caesar, G. D. McCarthy, D. J. R. Thornalley, N. Cahill, S. Rahmstorf, *Nat. Geosci.* **14**, 118-120 (2021). doi:10.1038/s41561-021-00699-z.

20. P. T. Spooner et al., *Geophys. Res. Lett.* **47**, e2020GL087577 (2020). doi:10.1029/2020GL087577.

21. R. Curry, C. Mauritzen, *Science* **308**, 1772-1774 (2005). doi:10.1126/science.1109477.

22. A. R. Friedman, G. Reverdin, M. Khodri, G. Gastineau, *Geophys. Res. Lett.* **44**, 1866-1876 (2017). doi:10.1002/2017GL072582.

23. Marine and Freshwater Research Institute Iceland, Marine measurements around Iceland. https://sjora.hafro.is/ (2022).

24. D. Roemmich et al., *Nat. Clim. Chang.* **5**, 240-245 (2015). doi:10.1038/nclimate2513.

25. G. Gebbie, P. Huybers, *Science* **363**, 70-74 (2019), doi:10.1126/science.aar8413.

26. D. Roemmich, W. J. Gould, J. Gilson, *Nat. Clim. Chang.* **2**, 425-428 (2012). doi:10.1038/nclimate1461.

27. N. P. McKay, D. S. Kaufman, *Sci. Data* **1**, 140026 (2014). doi:10.1038/sdata.2014.26.

28. M. B. Osman et al., *Nat. Geosci.* **14**, 756-761 (2021). doi:10.1038/s41561-021-00818-w.

29. B. L. Otto-Bliesner et al., *Bull. Am. Meteorol Soc.* **97**, 935-954 (2016). doi:10.1175/BAMS-D-14-00233.1.

30. M. W. Miles, C. S. Andresen, C. v. Dylmer, *Sci. Adv.* **6**, eaba4320 (2020). doi:10.1126/sciadv.aba4320.

31. M. Alonso-Garcia et al., *Clim. Past* **13**, 317-331 (2017). doi:10.5194/cp-13-317-2017.

32. A. Morley et al., *Earth Planet. Sci. Lett.* **308**, 161-171 (2011). doi:10.1016/j.epsl.2011.05.043.

33. D. Desbruyères, L. Chafik, G. Maze, *Commun. Earth Environ*. **2**, 48 (2021), doi:10.1038/s43247-021-00120-y.

34. D. J. R. Thornalley, H. Elderfield, I. N. McCave, *Nature* 457, 711-714 (2009). doi:10.1038/nature07717.

35. Z. Liu *et al.*, *Science* **325**, 310-314 (2009), doi:10.1126/science.1171041.

36. D. J. R. Thornalley et al., *Nature* **556**, 227-230 (2018). doi:10.1038/s41586-018-0007-4.

37. L. Caesar, S. Rahmstorf, A. Robinson, G. Feulner, V. Saba, *Nature* **556**, 191-196 (2018). doi:10.1038/s41586-018-0006-5.

38. A. Bower, H. Furey, *J. Geophys. Res. Oceans* **122**, 6989–7012 (2017). doi:10.1002/2017JC012698.

39. M. I. García-Ibáñez et al., *Prog. Oceanogr.* 135, 18-36 (2015). doi:10.1016/j.pocean.2015.03.009.

40. T. P. Boyer et al., World Ocean Atlas 2018 (Temperature and salinity). *NOAA National Centers for Environmental Information* (2018). (available at https://www.ncei.noaa.gov/products/world-ocean-atlas).

41. R. Schlitzer, Ocean Data View (2021). (available at https://odv.awi.de/).

42. P. Moffa-Sánchez, A. Born, I. R. Hall, D. J. R. Thornalley, S. Barker, *Nat. Geosci.* **7**, 275-278 (2014). doi:10.1038/ngeo2094.

Acknowledgments: We thank the WHOI Seafloor Samples Repository for curating the samples, and WHOI NOSAMS for radiocarbon analyses. We thank K. Pietro and S. Wang for technical assistance.

Funding: This work was funded by NSF grants OCE-2031929 (to G.G. and D.W.O.) and OCE-1304291 (to D.W.O. and D.J.R.T.) and by WHOI's Edna McConnell Clark Foundation Fund (to D.W.O.). W.L. was supported by the WHOI Postdoctoral Scholar Program, with funding provided by the Weston Howland Jr. Postdoctoral Scholarship, and by NSF OCE-2114579 (to D.W.O).

Author contributions:

Conceptualization: DWO, GG

Methodology: WL, DWO, GG

Investigation: WL, DWO, GG, DJRT

Visualization: WL, DWO

Funding acquisition: DWO, GG, DJRT, WL

Project administration: DWO

Supervision: DWO, GG

Writing – original draft: WL

Writing – review & editing: WL, DWO, GG, DJRT

Competing interests: The authors declare no competing interests.

Data and materials availability: Source data for Figs. 1-3, S6-S15 are provided in the supplementary materials. The raw radiocarbon, isotope data and R-scripts to reproduce the results are publicly available at the National Center for Environmental Data (https://www.ncei.noaa.gov/access/paleo-search/study/38185) and Zenodo repository (URL will be open to public upon acceptance).

Supplementary Materials

Materials and Methods

Supplementary Text

Figs. S1 to S21

Tables S1

Data S1-S4

References (*43–48*)

Fig. 1. Locations of eleven EN539 multicores along with schematic illustrations of ocean circulations (A), sea surface temperature (B), sea surface salinity (C), temperature (D), salinity (E), and $\delta^{18}O_{calcite}$ (F) sections along the eastern flank of Reykjanes Ridge. The isopycnal layers are shown in dashed lines in F), with the 27.8 kg/m^3 isopycnal defining the upper boundary of the ISOW plume (*38*). The ocean circulation paths were adapted from ref. (*39*), with thin red arrows showing warm salty surface Atlantic waters, thin green arrow showing cold fresh surface water sourced from Arctic, and thick dashed lines showing deep overflow pathways. Temperature and salinity data are the average of six decadal climatologies from 1955 to 2017 from the World Ocean Atlas 2018 (*40*). The $\delta^{18}O_{calcite}$ section was converted from an oceanographic data inversion (*10*) using empirical calibrations (*14*). The figures were generated using Ocean Data View software (*41*). SPG: Subpolar Gyre; NAC: North Atlantic Current; EGC: East Greenland Current; ISOW: Iceland-Scotland Overflow Water; DSOW: Denmark Strait Overflow Water; LSW: Labrador Sea Water; SPMW: Subpolar Mode Water.

Fig. 2. Planktic and benthic $\delta^{18}O$ records compared with global mean surface air temperature (GMST) history (*1*) **and temperature anomalies from the OPT-0015 inversion model** (*25*)**.** A) Global mean surface air temperature anomalies with respect to 1961–1990 CE. B)-D) 11 foraminiferal $\delta^{18}O$ records arranged by increasing core water depth. Thick colored lines correspond to the median $\delta^{18}O$ ensemble member, and colored shading shows the 90% highest-density probability ranges determined by R software package "geoChronR" (*16*) (Methods). To compare the modelled temperature trends (black dashed lines, OPT-0015) to the $\delta^{18}O$ changes, we scaled a 1°C decrease to correspond to a 0.22‰ $\delta^{18}O$ increase (*14*). Thick color-coded arrows indicate mean ensemble change point ages where they are significant, and cyan-colored bars

denote the ranges of these ages. Benthic records in MC28A, 26A, 25A were generated on *U. peregrina*, and the other benthic records were generated on *C. wuellerstorfi*.

Fig. 3. Change point (CP) estimates vs. $\delta^{18}O$ differences (after minus before the CP) in both $\delta^{18}O$ records and OPT-0015 inversion for the MCA-LIA transition (pre-1850 dataset) (A) and industrial era (post-1850 dataset) (B). Note that the y-axes are reversed. Points below the zero dashed line in A) imply colder saltier LIA conditions; points above the zero dashed line in B) imply warmer fresher post-1950s conditions. In the benthic records, open circles denote *U. peregrina*, closed circles denote *C. wuellerstorfi*. The *G. inflata* $\delta^{18}O$ record of nearby core RAPiD-17-5P is from ref. (*42*).

Fig. 4. Anomalous temperature evolution south of Iceland (grid box of 61.5°N, 20.5°W) from the OPT-0015 inversion (*25*) during the last 2,000 years (A) and from 1850 to 2015 CE (B).

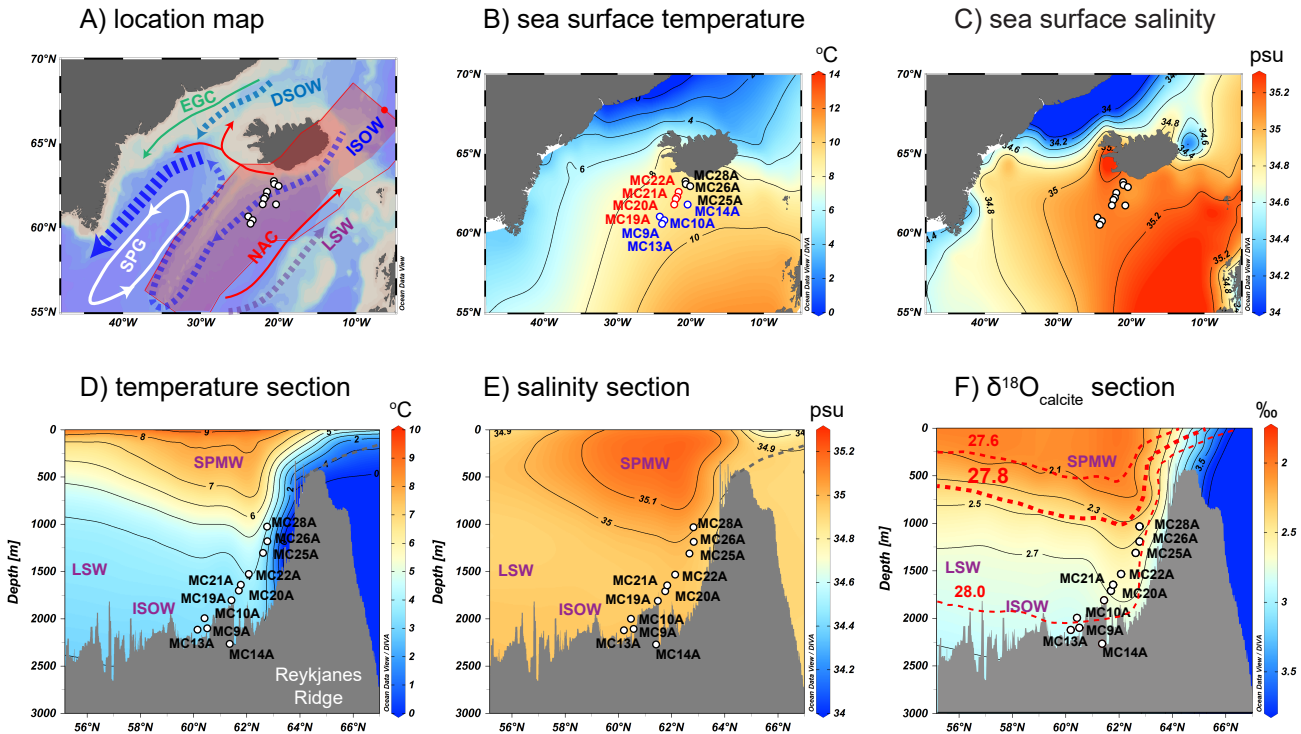
A) location map
EGC
DSOW
ISOW
SPG
NAC
LSW
B) sea surface temperature
°C
MC28A
MC26A
MC22A
MC21A
MC25A
MC20A
MC14A
MC19A
MC10A
MC9A
MC13A
C) sea surface salinity
psu
D) temperature section
°C
SPMW
LSW
ISOW
Reykjanes Ridge
Depth [m]
E) salinity section
psu
F) δ18Ocalcite section
‰
27.6
27.8
28.0
Ocean Data View / DIVA

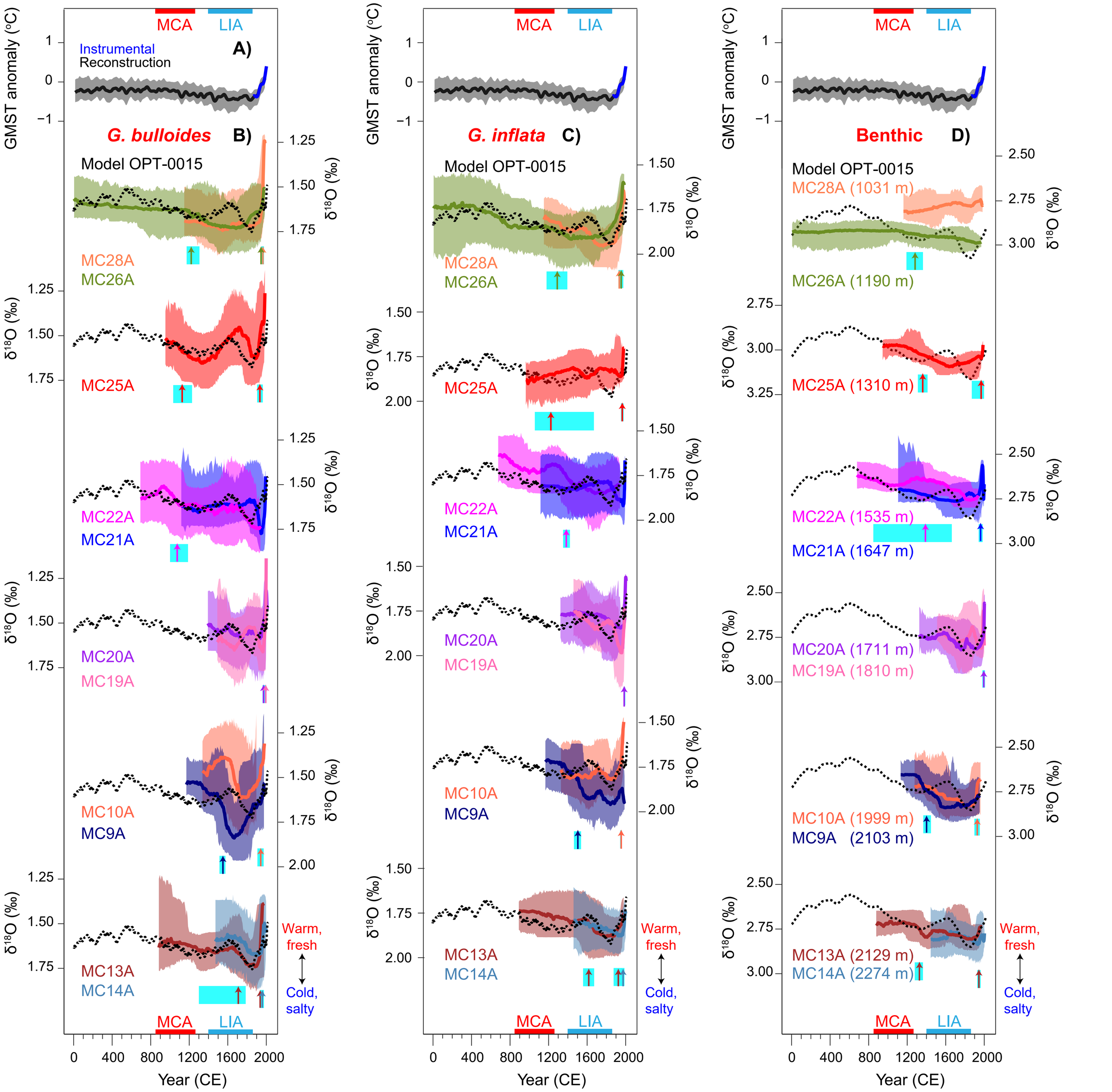
MCA
LIA
GMST anomaly (°C)
A)
Instrumental
Reconstruction
G. bulloides
B)
G. inflata
C)
Benthic
D)
Model OPT-0015
MC28A
MC26A
MC25A
MC22A
MC21A
MC20A
MC19A
MC10A
MC9A
MC13A
MC14A
MC28A (1031 m)
MC26A (1190 m)
MC25A (1310 m)
MC22A (1535 m)
MC21A (1647 m)
MC20A (1711 m)
MC19A (1810 m)
MC10A (1999 m)
MC9A (2103 m)
MC13A (2129 m)
MC14A (2274 m)
δ18O (‰)
Warm, fresh
Cold, salty
Year (CE)

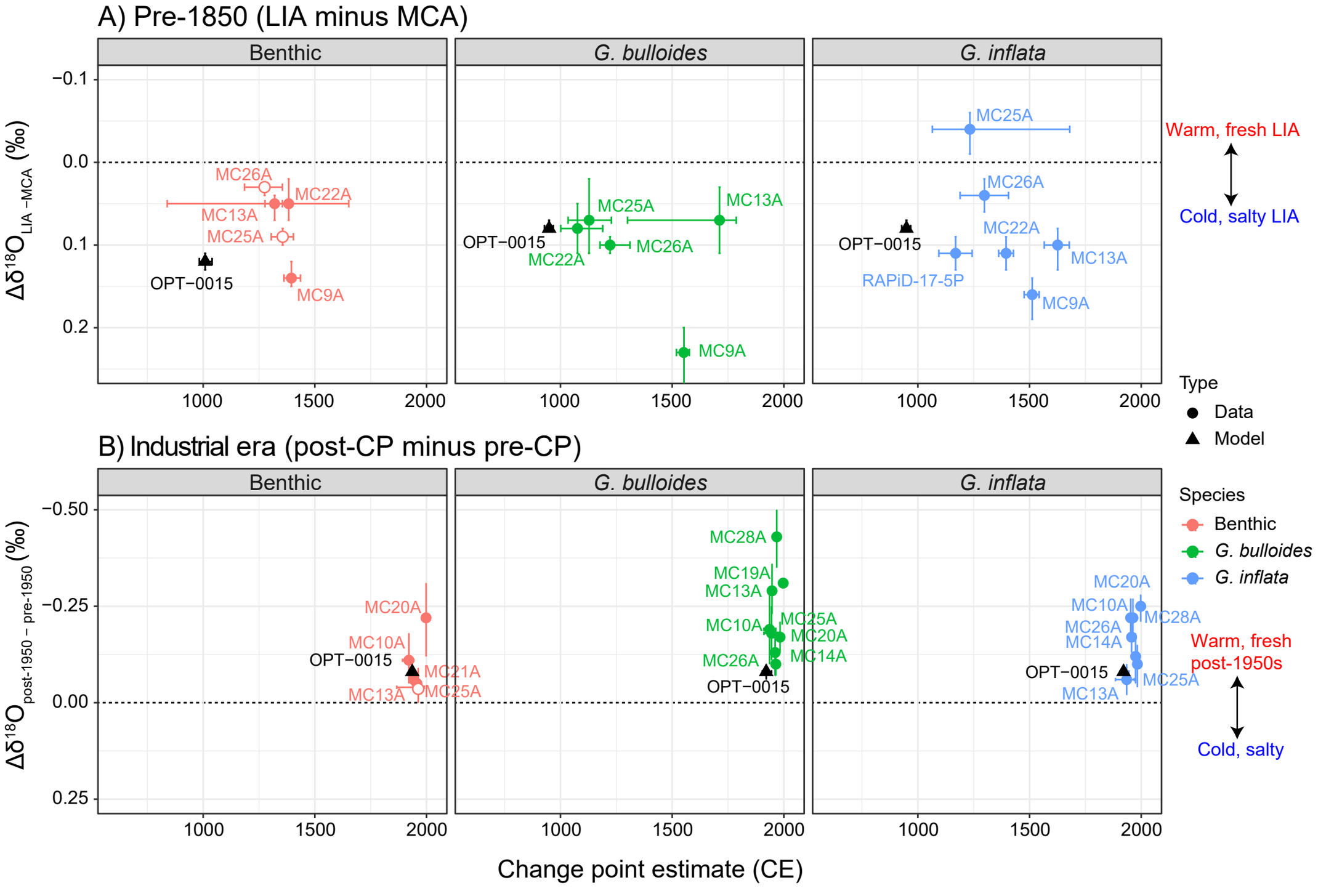
A) Pre-1850 (LIA minus MCA)
Benthic
G. bulloides
G. inflata
$\Delta\delta^{18}O_{LIA-MCA}$ (‰)
−0.1
0.0
0.1
0.2
MC26A
MC22A
MC13A
MC25A
OPT−0015
MC9A
MC25A
MC13A
OPT−0015
MC22A
MC26A
MC9A
MC25A
OPT−0015
MC22A
MC13A
RAPiD-17-5P
MC9A
1000
1500
2000
Warm, fresh LIA
Cold, salty LIA
Type
Data
Model
B) Industrial era (post-CP minus pre-CP)
Benthic
G. bulloides
G. inflata
$\Delta\delta^{18}O_{post-1950-pre-1950}$ (‰)
−0.50
−0.25
0.00
0.25
MC20A
MC10A
OPT−0015
MC21A
MC13A
MC25A
MC28A
MC19A
MC13A
MC10A
MC25A
MC20A
MC14A
MC26A
OPT−0015
MC20A
MC10A
MC28A
MC26A
MC14A
OPT−0015
MC25A
MC13A
1000
1500
2000
Species
Benthic
G. bulloides
G. inflata
Warm, fresh post-1950s
Cold, salty
Change point estimate (CE)

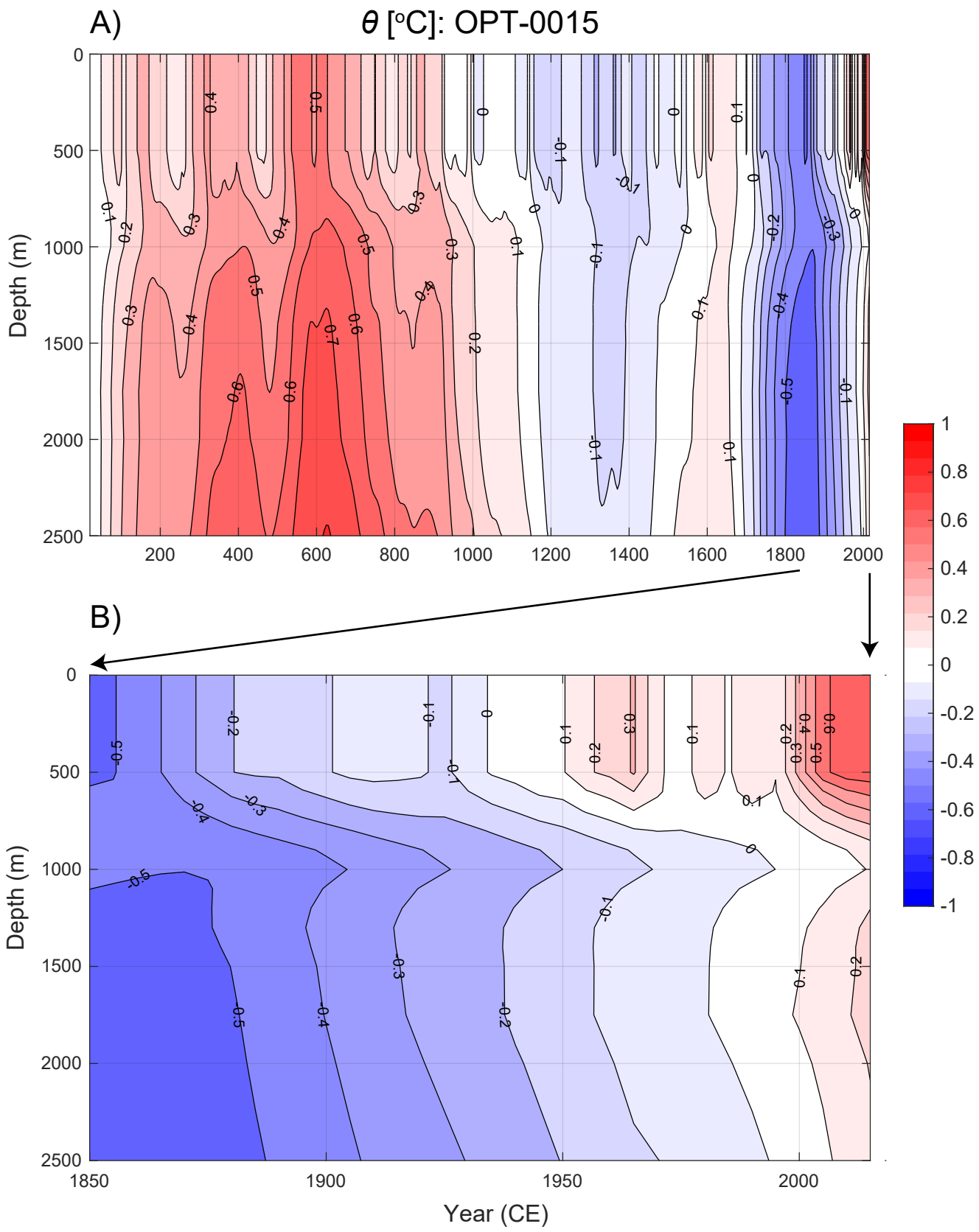
A)
θ [°C]: OPT-0015
Depth (m)
0
500
1000
1500
2000
2500
200
400
600
800
1000
1200
1400
1600
1800
2000
B)
Depth (m)
1850
1900
1950
2000
Year (CE)
1
0.8
0.6
0.4
0.2
0
-0.2
-0.4
-0.6
-0.8
-1

Science
AAAS

Supplementary Materials for

Surface climate signals transmitted rapidly to deep North Atlantic throughout last millennium

Wanyi Lu[1]*, Delia W. Oppo[1], Geoffrey Gebbie[1], David J. R. Thornalley [1,2]

[1] Woods Hole Oceanographic Institution, Woods Hole, MA, USA
[2] Department of Geography, University College London, London, UK

Correspondence to: wlu@whoi.edu

The PDF file includes:

Materials and Methods
Supplementary Text
Figs. S1 to S21
Tables S1
References

Other Supplementary Materials for this manuscript include the following:

Data S1-S4

Materials and Methods

Isotopic analyses

Multicores from 11 sites were sampled every 0.5 cm from top to bottom. Wet samples were first weighed and then oven- or freeze-dried. All dried samples were reweighed after drying in order to calculate water content in each sample. The sediments were then wet-sieved to > 63 μm fraction with de-ionized water, and oven-dried at 45°C. Planktic foraminifera *G. bulloides* and *G. inflata* were picked from the 250 – 355 μm fraction, and the benthic foraminifera *C. wuellerstorfi* and *U. peregrina* were picked from the > 212 μm fraction. Carbon and oxygen isotopic analyses were made using a Finnigan MAT253 mass spectrometer at the Woods Hole Oceanographic Institution (WHOI) with a laboratory precision (1σ) of the NBS-19 carbonate standard of ± 0.07 ‰ for $\delta^{18}O$ and ± 0.02 ‰ for $\delta^{13}C$ over the period of analyses. Each isotope analysis used 3 – 8 specimens of *G. bulloides*, 2 – 5 specimens of *G. inflata*, 1 – 5 specimens of *C. wuellerstorfi*, and 1 – 7 specimens of *U. peregrina*. We analyzed a total of 1,069 isotopes for *G. bulloides*, 943 isotopes for *G. inflata*, 439 isotopes for *U. peregrina*, and 461 isotopes for *C. wuellerstorfi*.

Age model development

Three to eight samples including samples from or near the top, middle, and bottom of the "A" core from each site were selected for radiocarbon dating. Each radiocarbon date represents an average of 100 – 450 individuals of *G. bulloides*, picked from the > 250 or > 300 μm size fractions. All accelerator mass spectrometry (AMS) ^{14}C dates were acquired at the National Ocean Sciences Accelerator Mass Spectrometry facility at WHOI. Planktic ^{14}C dates were calibrated against Marine20 using Calib8.20 (*43*) and a regional marine radiocarbon reservoir age correction ΔR = -108 and uncertainty of 40 years (*44*).

Except for MC13A and MC22A, the radiocarbon fraction modern (Fm) in all core-top samples (0-0.5 cm) is >1, which is outside of the calibration curve of Marine20 and thus requires manual age assignment. The Fm shows a significant negative correlation with $\delta^{13}C$ measured in the same sample ($R^2 = 0.73$, $p < 0.01$) (Table S1), suggesting that more modern sediments (larger Fm) have lower $\delta^{13}C$, consistent with a larger Suess effect (*17*). We used this negative correlation to guide the core-top sample age assignment: core-top samples with higher Fm and lower $\delta^{13}C$ should have younger ages than those with lower Fm. We first assigned the core-top sample of MC20A, having the highest Fm, to year 2010, and the core-top sample age of core MC22A, with the lowest Fm, to 1970. We then applied a simple linear fit between these Fm values and assigned ages of these two cores, and calculated the age of the core-top sample of all other dated cores based on their Fm. An exception was made for core MC13A because this core-top sample has Fm < 1 but shows a clear planktic $\delta^{13}C$ decrease close to the top (note no apparent benthic $\delta^{13}C$ decrease) (Fig. S9 and S11). Because the amplitude of the planktic $\delta^{13}C$ decrease is similar to MC10A, we assigned the core-top sample age of MC13A to 1988, the same as MC10A. Except for MC22A, the age uncertainty of all core-top sample ages was assigned to be 1 year. We did not assign 2014 (when the sampling cruise took place) as the youngest core-top sample age, because doing so gave median Bayesian ages younger than 2014 in a small portion of samples. Moreover, bioturbation mixes the upper sediment, and so a collection age assignment at 0 – 0.5 cm is unrealistic.

The age models were constructed using the BACON package in R (*45*), which uses Bayesian statistics to reconstruct accumulation histories for deposits based on radiocarbon data and the core-top sample age assignment. We further used the top and bottom median age from BACON output to construct simple age models for each core, assuming constant dry-mass

accumulation rate throughout each core. The simple age models are consistent with the median age curves of the BACON models, with ages falling within the minimum and maximum 95% confidence age of BACON model (Fig. S4). The ^{210}Pb activity was previously analyzed in the top 10 cm of cores MC14A and 20A (*20*), providing additional independent accumulation rates for young sediments, which are also consistent with our age models. We use the BACON age models as they take age uncertainty into account.

At several sites, we also conducted analyses on a second subcore from the same multicore sampling deployment. Specifically, we also collected isotope data and pumice abundances on the MC14 B subcore (MC14B), and faunal counts on MC14B, MC14G, MC9B and MC10F. Because no ^{14}C dates were collected on these subcores, we aligned the cores to the A core as follows: we assumed the sub-core experienced the same dry mass accumulation rate as the A-core, and then we calculated the ages in the sub-core using the dry mass in each sample. We next fit a linear regression between the median ensemble age and depth in the A-core to estimate age for the subcore. In the case of MC14, where we combined data from several subcores, we used the linear fit equation and the median ages in the subcore to calculate "corrected" sampling depths for the subcore (Data S2). We used "corrected" sampling depths for the subcores to combine with data from the A-core to produce one time series and used the combined data as input for geoChronR, described below.

Age uncertainty analyses

Quantifying chronological uncertainty is important for our analyses. We used an R package "geoChronR" to model, analyze, and visualize the age-uncertain isotope data (*16*). For each core (or combined cores in the case of MC14), we first created an age model using runBacon function, then created 1,000 age-uncertain δ^{18}O ensembles in each core, computed the median ensemble member and 50% and 90% highest-density probability range, and exported the ensemble series using plotTimeseriesEnsRibbons and plotTimeseriesEnsLines functions. The plotting of outliers on the year axis was set to exclude values below 5% and 95% probability limit (limit.outliers.x = 0.025). The number of bins over which to calculate intervals (nbin) was separately calculated for each core based on the approximate age span of the core, in order to obtain an approximate 5-year age interval (Table S1).

The binning procedure in "geoChronR" sets up a binning interval, which is typically evenly spaced every 5 years. However, the actual length of the bin varies from ~ 5 to 10 years (Data S3). For each nominal 5-year bin, the median, 50%, and 90% highest probability ranges of data are calculated. This intentionally degrades the median resolution of the timeseries and smooths the data. The binning procedure is repeated for each of 1,000 ensemble members, meaning that between different ensembles, different observations (in our case, isotope data) will be placed in different 5-year bins. We used MC25A benthic δ^{18}O dataset as an example to visualize the age-uncertain data (Fig. S5A-B). Note that on Fig. S5B, we only plot each raw data point once, on its median BACON age, to illustrate the approximate sampling resolution in the age domain.

We selected four 20-year bins to visualize the age-uncertain δ^{18}O data distribution (note that we used 20-year bins instead of 5-year bins because doing so would allow more than one raw δ^{18}O sample with their median BACON ages falling into the 20-year bins). In some bin intervals (e.g., 1000-1020 and 1900-1920 CE), the median δ^{18}O ensemble (blue) is lower than the mean of raw δ^{18}O data (pink) on their median BACON ages (Fig. S5C). This is because there are many other observations falling into the bins (open symbols). We extracted those possible observations in each 20-year bin based on the average age error (2σ) in each sample (approximately ± 150

years at 1010 and 1540 CE; approximately ± 100 years at 1910 CE; and approximately ± 40 years at 1970 CE, Fig. S4), and plot the possibility distribution of $\delta^{18}O$ values falling within the 20-year bin. Thus, the probability distributions are multimodal and the median (blue) and mean (pink) may differ significantly.

Change point analyses

To determine whether there were significant changes in the mean of $\delta^{18}O$ and $\delta^{13}C$ in the records, we adapted a method that was previously used to detect AMOC strength change in the last 1,000 years (*19*). The approach uses a Bayesian framework that assumes the data fluctuate around a constant mean, allowing for a single change in the mean at some point in time, thus taking both data uncertainty and data variability into account (regardless of the origin of the data variability). Because we identified two change points in the $\delta^{18}O$ time series (one near the MCA-LIA transition, the other one around ~1900), we divided the ensemble time series of each record into pre-1850 and post-1850 datasets to calculate two change points. We only performed analysis on pre-1850 dataset in the six cores with bottom median BACON ages older than 1200 CE (MC26A, 25A, 22A, 21A, 9A, 13A), and in the composite records which also only include data from these six cores. We also did not perform analysis on the post-1850 dataset in MC22A because its core-top sample ^{14}C has a pre-bomb age.

We used the median $\delta^{18}O$ (or $\delta^{13}C$) ensemble and 90% highest-density probability ranges in each individual core (Fig. S6-11), and the mean and standard deviation of the smoothed composite records (Fig. S14), as mean and uncertainty inputs. If the model identified a change point (CP), that is, a difference in the mean across the time interval, we computed the $\delta^{18}O$ difference before and after the CP. If the 95% Bayesian credible interval of $\delta^{18}O$ difference shows opposite signs, we assumed no significant $\delta^{18}O$ changes in that core. We additionally performed change point analyses on OPT-0015 inversion results (Fig. S20) (*25*), Arctic temperature reconstruction (*27*), and Greenland ice cap growth records (*28*).

For the five records passing the pre-1850 change point significance tests (Fig. 3), four records (MC26A, 25A, 22A, 13A) have bottom median BACON ages older than 1000 CE, thus covering at least half of MCA interval (Table S1). As MC9A has the shortest record with a bottom age of ~1200 CE, thus lacking most of MCA interval, the resulting change points may be too young.

We performed Levene's tests on the change point ages between benthics versus planktics to assess whether the MCA-LIA change points have the same variance between groups. The statistical results indicate the *p*-value is 0.08 for benthic vs. *G. bulloides*, and 0.04 for benthic vs. *G. inflata*, suggesting the change point spreads in planktic $\delta^{18}O$ are significantly different than that of benthic $\delta^{18}O$ at the 90% confidence interval.

Supplementary text

Potential impact of bioturbation on change point results

Marine sediment records can be impacted by bioturbation which can modify signals after deposition. At site MC14A and B, the pumice abundance (from > 355 μm fraction) peaks at 5.75 cm (adjusted depth for MC14B), which is believed to derive from the 1947 Hekla volcanic eruption (Fig. S16). This tephra layer independently supports the results of BACON age model (median age of 1934 CE, with 95% confidence age range between 1794 and 1989 CE), which was only constrained by radiocarbon dates and assumed slowly changing accumulation rates. The pumice peak signal occurs over an ~5 cm interval, suggesting tephra reworking by

bioturbation. Bioturbation may have also altered the faunal abundance signal in the top 5 cm of sediments (Fig. S16). Specifically, there is a greater abundance of the species used for isotope analyses in the top two cm of the core than in the next deepest two cm. Thus specimens found at 2 - 4 cm could have been mixed from 0 - 2 cm. In cores where this occurred, the actual change point of $\delta^{18}O$ and $\delta^{13}C$ records in the industrial era would have been even younger than the current estimates. Thus, the true change point may be younger than our average estimate of 1964 CE.

Because *G. bulloides* and *G. inflata* abundance data are only available at site MC14 and the bottom sample of MC14 does not extend to the MCA interval, we do not have conclusive evidence of bioturbation impact on planktic MCA – LIA change point results. However, as planktic foraminifera responds to changes in environmental conditions such as temperature and nutrients, faunal changes across this transition are likely to occur. Bioturbation coupled with abundance changes may have also affected the change points of the planktic records. Furthermore, spatial differences in surface changes (and hence planktic faunal abundance changes) across our sites, larger surface seasonal variability and depth habitat changes of planktic foraminifera, coupled with differential bioturbation may have contributed to the large range in estimates of planktic $\delta^{18}O$ change points. On the other hand, benthic abundances at the five sites (MC26A, 25A, 22A, 9A, 13A showing significant benthic $\delta^{18}O$ changes across MCA - LIA, Fig. 3), do not show significant abundance changes near the MCA- LIA change point (Fig. S17), suggesting that bioturbation should have had a relatively small impact on the benthic MCA -LIA change point results, also consistent with their relatively narrow range.

Ocean circulation model

The Common Era inversion and water-mass diagnostics utilize an ocean circulation model derived from the Total Matrix Intercomparison method (*10*). This ocean circulation is represented by a matrix, A, whose elements are filled with advective and diffusive fluxes that are inferred from observations collected during the World Ocean Circulation Experiment (WOCE) of the 1990s. Distributions of temperature, salinity, nutrients, oxygen, and radiocarbon are inverted such that A respects conservation equations for mass and all observed properties. Circulation is represented at 2-degree horizontal resolution across 33 vertical layers, leading to 291,156 grid cells and A having this dimension squared. The model is driven by providing the temperature of waters subducted below the surface mixed layer, which is best interpreted as the average sea-surface temperature over the three coldest months of the year (*46*). Thus, the ocean circulation model tracks the passive response of the ocean interior to SST, but does not permit the influence of temperature on density to be felt.

We diagnose water-mass fractions and ventilation ages by interpolating the circulation model characteristics onto the EN539 core sites. Three water masses are defined by the surface origin of seawater: GIN (Greenland-Iceland-Norwegian Sea water), LSW (Labrador Sea Water), and SPMW (Subpolar Mode Water). The GIN region is defined to be north of the Greenland-Iceland-Scotland ridge and is the origin of Denmark Strait Overflow Water (DSOW) and ISOW. Our water masses labeled LSW and SPMW originate from south of the ridge and north of the Gulf Stream and North Atlantic Current, respectively. LSW and SPMW are distinguished by the 0.4 spiciness level as referenced to 0 dbar following ref. (*47*). In particular, SPMW is spicier than 0.4 and LSW is less spicy than this value. This value of spiciness corresponds to a boundary between LSW and SPMW at about 4.5 °C and 35.0 psu. With this definition, Irminger Sea Water

is included as a SPMW, and is the least spicy (i.e., freshest) component of this water mass.

OPT-0015 solution for the Common Era

The inverse model formulation that was used to create the OPT-0015 Common Era solution (*25*) is briefly recapitulated here. The inversion combines time-evolving observations with an ocean circulation model (discussed above) that is assumed constant in time. The solution is an "optimal" combination of observations and model starting in the year 15 CE, and thus is referred to as OPT-0015 to be distinguished from a model simulation that is not constrained by data.

The inversion starts with a first guess solution derived by running the model with a first guess of Common Era SST. Here the first-guess SST takes an average of the 57 Ocean2k timeseries (*6*) and defines this to be the global-mean SST. After 1870, the Ocean2k dataset is blended with the HadISST1 instrumental data product to estimate the global-mean SST up to 2015. Then the inversion is started with the approximation that all 14 surface regions have a first-guess SST evolution that is equal to the global-mean SST. The location of the Ocean2k cores is not taken into account in this calculation.

Additional data constraints include subsurface temperature information from the HMS Challenger in the 1870s (*26*) and the World Ocean Circulation Experiment in the 1990s. The result of the inversion is a three-dimensional, global, time-evolving reconstruction of potential temperature for the years 15 - 2015 CE. While other tracers were used to derive the ocean circulation matrix, they were not used in the inversion for the Common Era evolution. Thus, the OPT-0015 solution does not contain any information about the evolution of salinity or seawater $\delta^{18}O$ ratios.

References and Notes

1. R. Neukom *et al.*, *Nat Geosci*. **12**, 643-649 (2019), doi:10.1038/s41561-019-0400-0.
2. S. Levitus et al., *Geophys. Res. Lett.* **39**, L10603 (2012). doi:10.1029/2012GL051106.
3. G. A. Meehl, J. M. Arblaster, J. T. Fasullo, A. Hu, K. E. Trenberth, *Nat. Clim. Chang.* **1**, 360–364 (2011). doi:10.1038/nclimate1229.
4. X. Chen, K. K. Tung, *Science* **345**, 897-903 (2014). doi:10.1126/science.1254937.
5. M.-J. Messias, H. Mercier, *Commun. Earth Environ*. **3**, 118 (2022). doi:10.1038/s43247-022-00443-4.
6. H. v. McGregor et al., *Nat. Geosci.* **8**, 671–677 (2015). doi:10.1038/ngeo2510.
7. B. Dickson et al., *Nature* **416**, 832-835 (2002). doi:10.1038/416832a.
8. P. Moffa-Sánchez et al., *Paleoceanogr. Paleoclimatol.* **34**, 1399-1436 (2019). doi:10.1029/2018PA003508.
9. H. R. Langehaug et al., *Paleoceanography*. **31**, 399–415 (2016). doi:10.1002/2015PA002920.
10. G. Gebbie, P. Huybers, *J Phys. Oceanogr.* **42**, 291-305 (2012). doi:10.1175/JPO-D-11-043.1.
11. T. Rossby, L. Chafik, L. Houpert, *Geophys. Res. Lett.* **47**, e2020GL087456 (2020). doi:10.1029/2020GL087456.
12. L. Jonkers, S. van Heuven, R. Zahn, F. J. C. Peeters, *Paleoceanography* **28**, 164-174 (2013). doi:10.1002/palo.20018.
13. A. Rebotim et al., *J. Micropalaeontol.* **38**, 113-131 (2019). doi:10.5194/jm-38-113-2019.
14. T. M. Marchitto et al., *Geochim. Cosmochim. Acta.* **130**, 1-11 (2014). doi:10.1016/j.gca.2013.12.034.
15. G. A. Schmidt, G. R. Bigg, E. J. Rohling, Global Seawater Oxygen-18 Database - v1.22 (1999). (available at https://data.giss.nasa.gov/o18data/)
16. N. P. McKay, J. Emile-Geay, D. Khider, *Geochronology* **3**, 149-169 (2021). doi:10.5194/gchron-3-149-2021.
17. C. D. Keeling, *Environ. Int.* **2**, 229-300 (1979). doi:10.1016/0160-4120(79)90005-9.
18. M. Eide, A. Olsen, U. S. Ninnemann, T. Eldevik, *Global Biogeochem. Cycles* **31**, 492-514 (2017). doi:10.1002/2016GB005472.
19. L. Caesar, G. D. McCarthy, D. J. R. Thornalley, N. Cahill, S. Rahmstorf, *Nat. Geosci.* **14**, 118-120 (2021). doi:10.1038/s41561-021-00699-z.
20. P. T. Spooner et al., *Geophys. Res. Lett.* **47**, e2020GL087577 (2020). doi:10.1029/2020GL087577.
21. R. Curry, C. Mauritzen, *Science* **308**, 1772-1774 (2005). doi:10.1126/science.1109477.
22. A. R. Friedman, G. Reverdin, M. Khodri, G. Gastineau, *Geophys. Res. Lett.* **44**, 1866-1876 (2017). doi:10.1002/2017GL072582.

23. Marine and Freshwater Research Institute Iceland, Marine measurements around Iceland. https://sjora.hafro.is/ (2022).

24. D. Roemmich et al., *Nat. Clim. Chang.* **5**, 240-245 (2015). doi:10.1038/nclimate2513.

25. G. Gebbie, P. Huybers, *Science* **363**, 70-74 (2019), doi:10.1126/science.aar8413.

26. D. Roemmich, W. J. Gould, J. Gilson, *Nat. Clim. Chang.* **2**, 425-428 (2012). doi:10.1038/nclimate1461.

27. N. P. McKay, D. S. Kaufman, *Sci. Data* **1**, 140026 (2014). doi:10.1038/sdata.2014.26.

28. M. B. Osman et al., *Nat. Geosci.* **14**, 756-761 (2021). doi:10.1038/s41561-021-00818-w.

29. B. L. Otto-Bliesner et al., *Bull. Am. Meteorol Soc.* **97**, 935-954 (2016). doi:10.1175/BAMS-D-14-00233.1.

30. M. W. Miles, C. S. Andresen, C. v. Dylmer, *Sci. Adv.* **6**, eaba4320 (2020). doi:10.1126/sciadv.aba4320.

31. M. Alonso-Garcia et al., *Clim. Past* **13**, 317-331 (2017). doi:10.5194/cp-13-317-2017.

32. A. Morley et al., *Earth Planet. Sci. Lett.* **308**, 161-171 (2011). doi:10.1016/j.epsl.2011.05.043.

33. D. Desbruyères, L. Chafik, G. Maze, *Commun. Earth Environ*. **2**, 48 (2021), doi:10.1038/s43247-021-00120-y.

34. D. J. R. Thornalley, H. Elderfield, I. N. McCave, *Nature* 457, 711-714 (2009). doi:10.1038/nature07717.

35. Z. Liu *et al.*, *Science* **325**, 310-314 (2009), doi:10.1126/science.1171041.

36. D. J. R. Thornalley et al., *Nature* **556**, 227-230 (2018). doi:10.1038/s41586-018-0007-4.

37. L. Caesar, S. Rahmstorf, A. Robinson, G. Feulner, V. Saba, *Nature* **556**, 191-196 (2018). doi:10.1038/s41586-018-0006-5.

38. A. Bower, H. Furey, *J. Geophys. Res. Oceans* **122**, 6989–7012 (2017). doi:10.1002/2017JC012698.

39. M. I. García-Ibáñez et al., *Prog. Oceanogr.* **135**, 18-36 (2015). doi:10.1016/j.pocean.2015.03.009.

40. T. P. Boyer et al., World Ocean Atlas 2018 (Temperature and salinity). *NOAA National Centers for Environmental Information* (2018). (available at https://www.ncei.noaa.gov/products/world-ocean-atlas).

41. R. Schlitzer, Ocean Data View (2021). (available at https://odv.awi.de/).

42. P. Moffa-Sánchez, A. Born, I. R. Hall, D. J. R. Thornalley, S. Barker, *Nat. Geosci*. **7**, 275-278 (2014). doi:10.1038/ngeo2094.

43. M. Stuiver, P. Reimer, R. Reimer, CALIB 8.2. http://calib.org (2022).

44. T. J. Heaton et al., *Radiocarbon* **62**, 779-820 (2020). doi:10.1017/RDC.2020.68.

45. M. Blaauw, J. A. Christen, *Bayesian Anal.* **6**, 457-474 (2011). doi:10.1214/11-BA618.

46. R. Williams, J. C. Marshall, M. A. Spall, *J Phys Oceanogr*. **25**, 3089–3102 (1995). doi: 10.1175/1520-0485(1995)025<3089:DSMLW>2.0.CO;2.

47. T. J. McDougall, O. A. Krzysik, *J Mar Res.* **73**, 141–152 (2015). doi: 10.1357/002224015816665589.

48. R. R. Dickson, J. Meincke, S. A. Malmberg, A. J. Lee, *Prog Oceanogr*. **20**, 103–151 (1988). doi: 10.1016/0079-6611(88)90049-3.

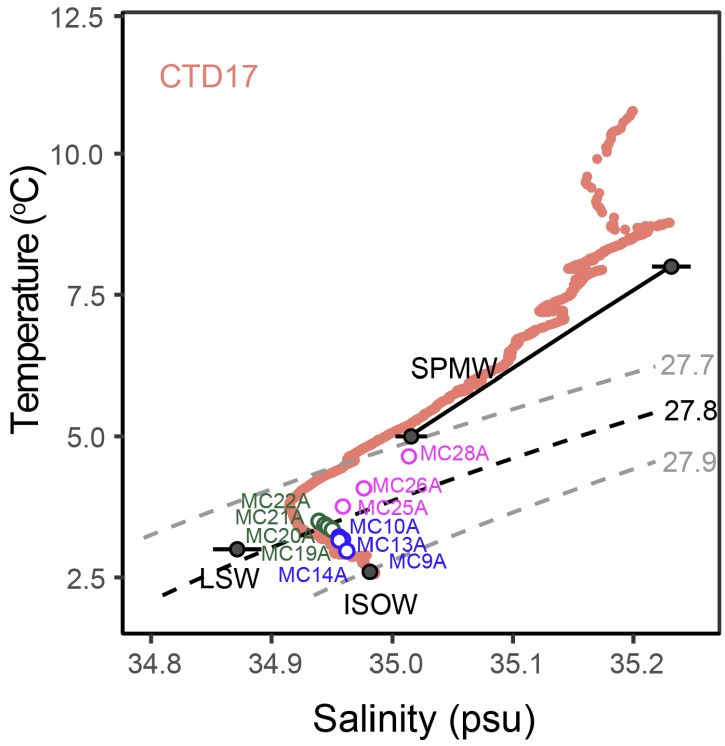

Fig. S1. Temperature-salinity (T-S) data collected on one EN539 CTD (conductivity, temperature, and depth profiler) deployment and of each multicore extracted from the TMI model results (Fig. S2). The T-S signatures of source water types are from ref. (*39*). CTD17 was deployed ~ 1°E of MC14A (61.48ºN, 19.54ºW). The dashed lines represent isopycnals, with the black one highlighting the 27.8 kg/m^3 isopycnal, which defines the upper boundary of the ISOW plume (*38*). SPMW ranges from the freshest vintage formed in the Irminger Sea to the saltiest formed in Iceland Basin. Pink, green and blue symbols refer to eleven EN539 multicores.

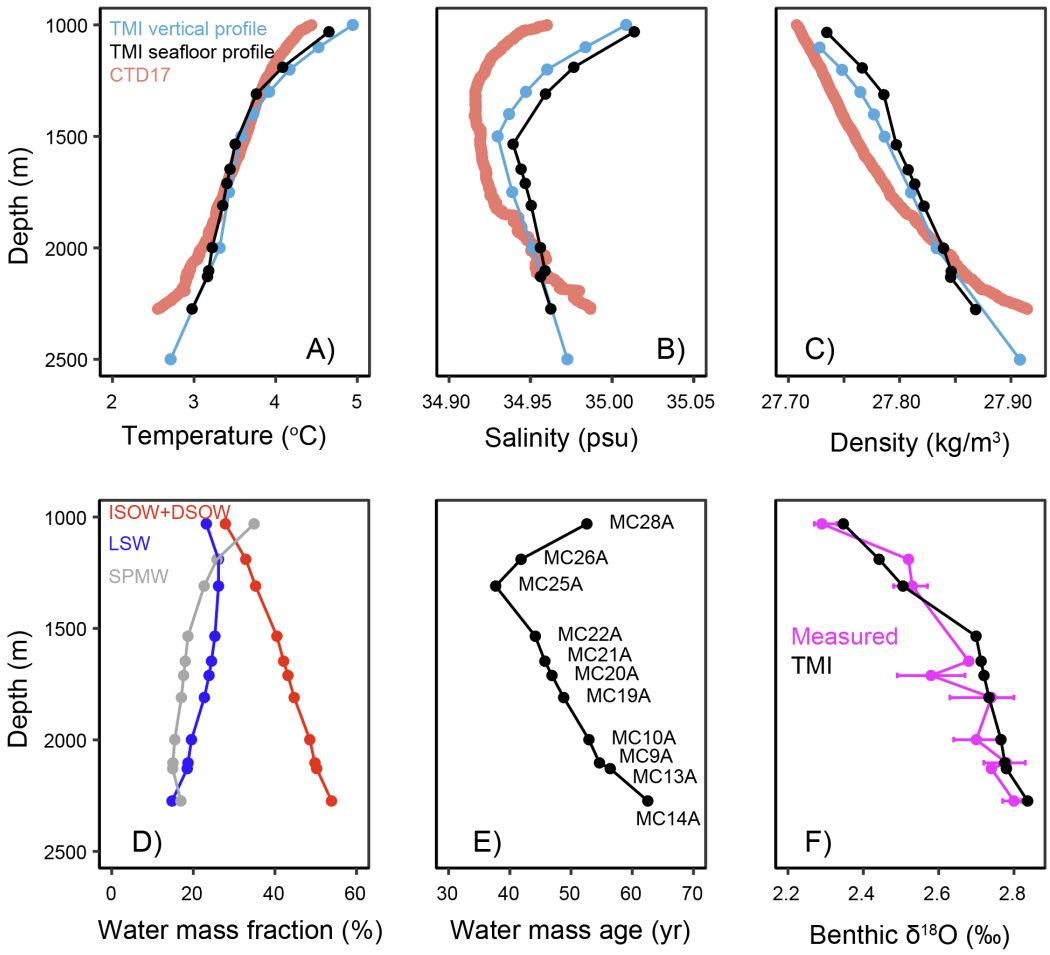

Fig. S2. Temperature, salinity, density (A-C), water mass fractions (D), mean ages (E), and $\delta^{18}O_{calcite}$ profiles extracted from the TMI model results (*10*) , along with salinity, temperature and density determined from a CTD deployment on cruise EN539 (Fig. S1), and modern measured benthic $\delta^{18}O$ values (median BACON ages between ~1920 and 2010 CE). In A-C, the seafloor profiles are the TMI properties interpolated to the core site, whereas the vertical profile is the water column profile at the site of the CTD deployment. We use TMI seafloor profiles in D-E. Except for the shallowest site, overflows contribute most to the water-mass mixture, becoming increasingly more dominant with increasing water depth (note that the TMI calculation did not distinguish ISOW and DSOW, but we assume this component contains mostly ISOW at our sites). The contribution of SPMW decreases with depth but slightly reverses at the deepest site. The LSW water mass fraction is nearly constant with depth, peaking at ~ 1300-1500 m. The mean ventilation ages at all core sites are < 70 years, implying that high-latitude surface signals are transmitted to depth. Differences between the TMI temperature and salinity vertical profiles and data from the cruise CTDs likely reflect the difference between the mean state over several decades of observations and a snapshot taken during the coring cruise.

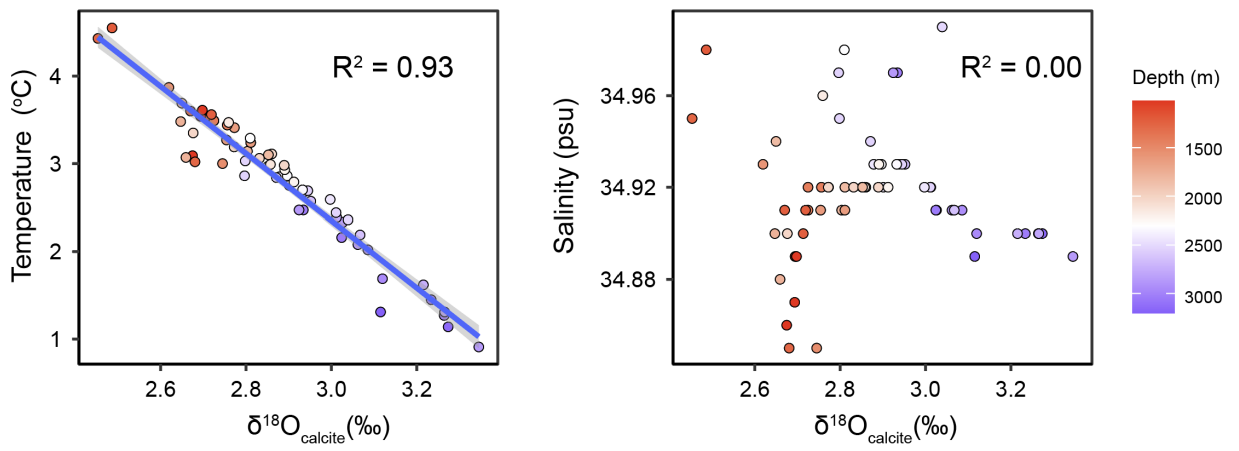

Fig. S3. Cross-plot of the predicted modern $\delta^{18}O_{calcite}$ vs. seawater temperature (A) and salinity (B) in deep subpolar North Atlantic below 1000 m. The modern observations of seawater temperature, salinity, and $\delta^{18}O$ (longitude between 5°W and 40°W, and latitude between 55°N and 63°N) were extracted from the Global Seawater Oxygen-18 Database (*15*). We converted seawater temperature and $\delta^{18}O$ to predict $\delta^{18}O_{calcite}$ using empirical calibrations (*14*). Our core sites are located along the eastern flank of Reykjanes Ridge and span water depths ~1000 – 2300 m (red and white colors), where the correlation between $\delta^{18}O_{calcite}$ and temperature is much stronger than that between $\delta^{18}O_{calcite}$ and salinity.

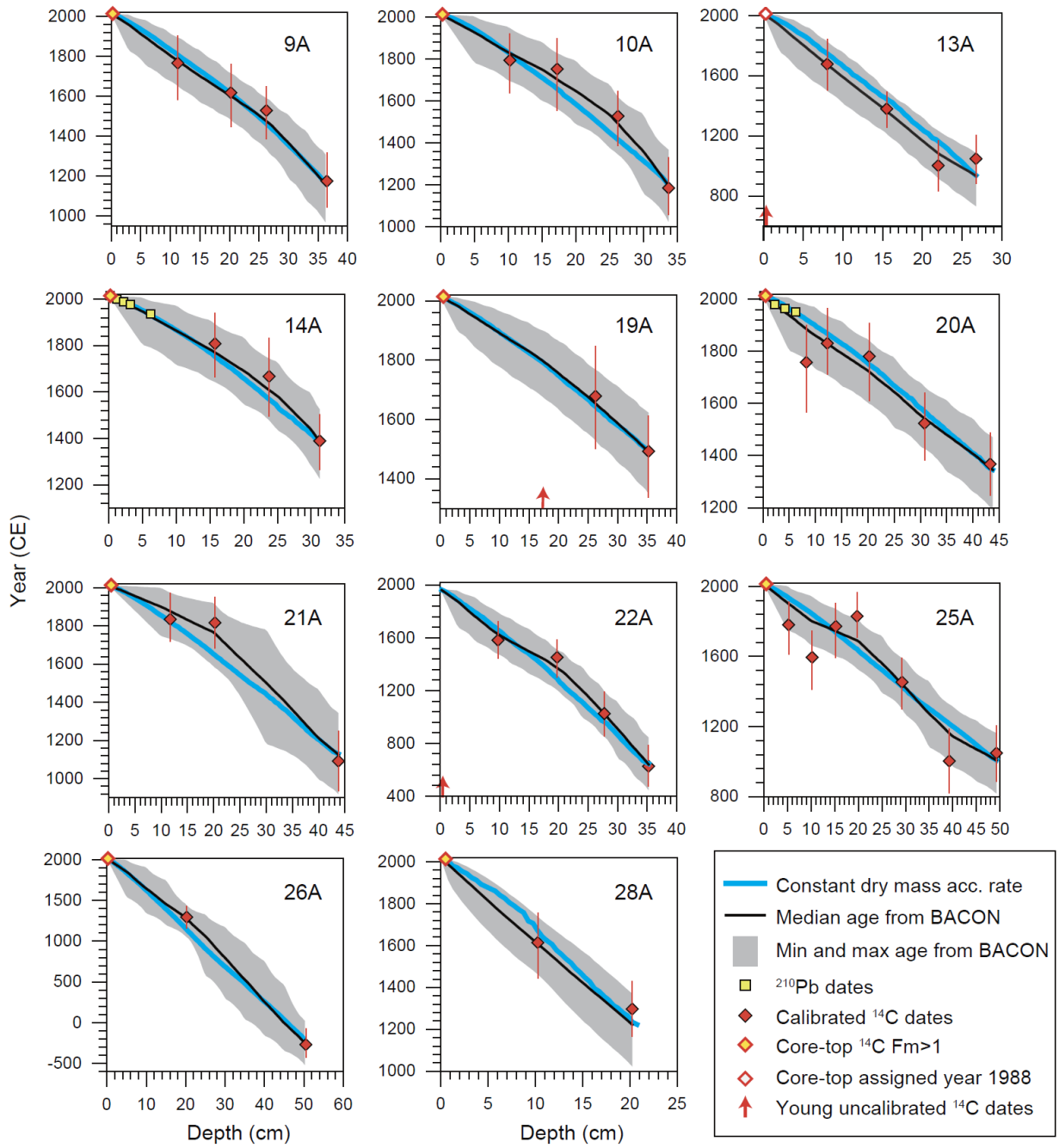

Fig. S4. Age models for EN539 multicores. The BACON age model is consistent with the simple age model assuming constant dry-mass accumulation rate and with ^{210}Pb-based accumulation rates. Error bars of each calibrated ^{14}C date denote 2σ uncertainty. All but one core (MC22A) shows a planktic δ^{13}C decrease near the top (Fig. S12), providing independent support for modern core-top ages. We used the BACON age models as they provide age uncertainties.

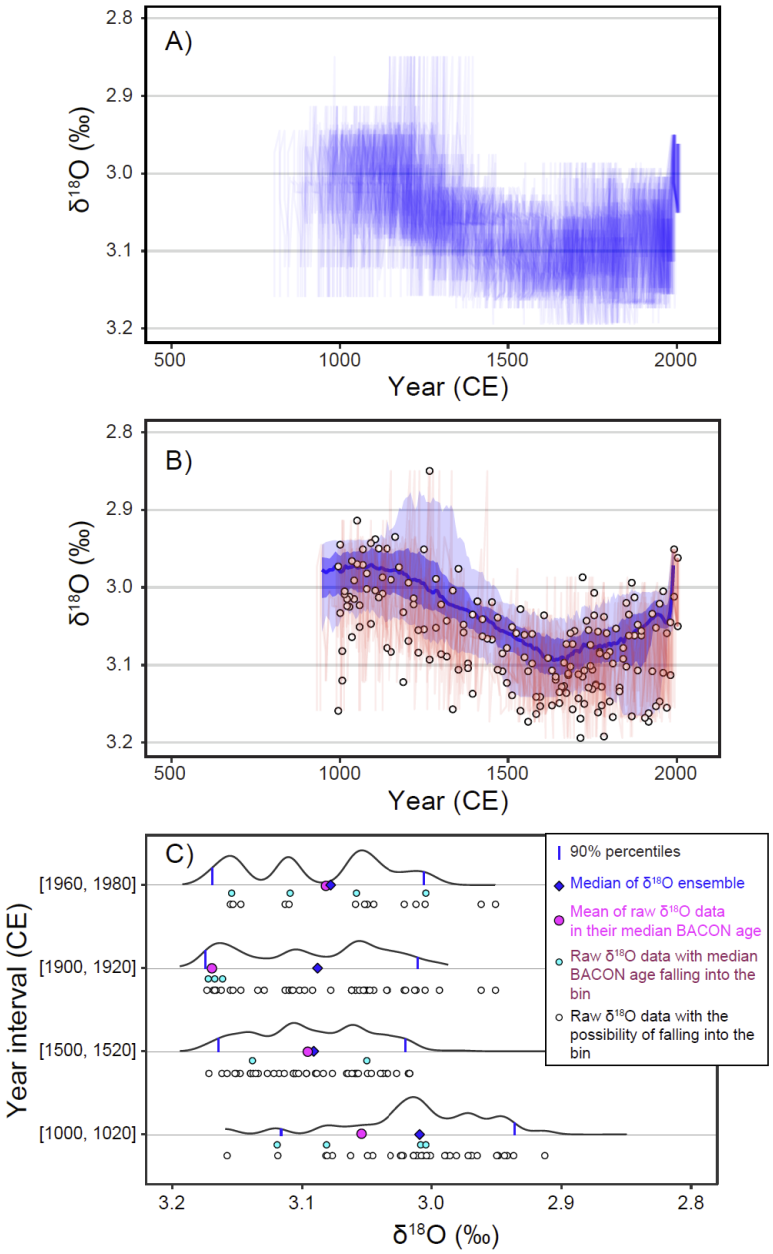

Fig. S5. An example of using geoChronR (*16*) to analyze and visualize age-uncertain data using the MC25A benthic $\delta^{18}O$ dataset. A) thin blue lines show 50 random ensemble members of $\delta^{18}O$ time-series data. B) thick blue line shows the median ensemble member; dark and light blue shadings show the 50% and 90% highest-density probability ranges, respectively; thin red lines show 5 random age-uncertain $\delta^{18}O$ ensemble members; open circles denote raw $\delta^{18}O$ data plotted on their median BACON age. C) violin plots to visualize data distribution in four bin intervals of the 1000 benthic $\delta^{18}O$ ensembles. This figure shows that the median of the $\delta^{18}O$ ensemble is close to the median of all data that can fall in the bin (open circles), and is often different from the median of the raw data (cyan circles) that fall in the bin if their median BACON age is used.

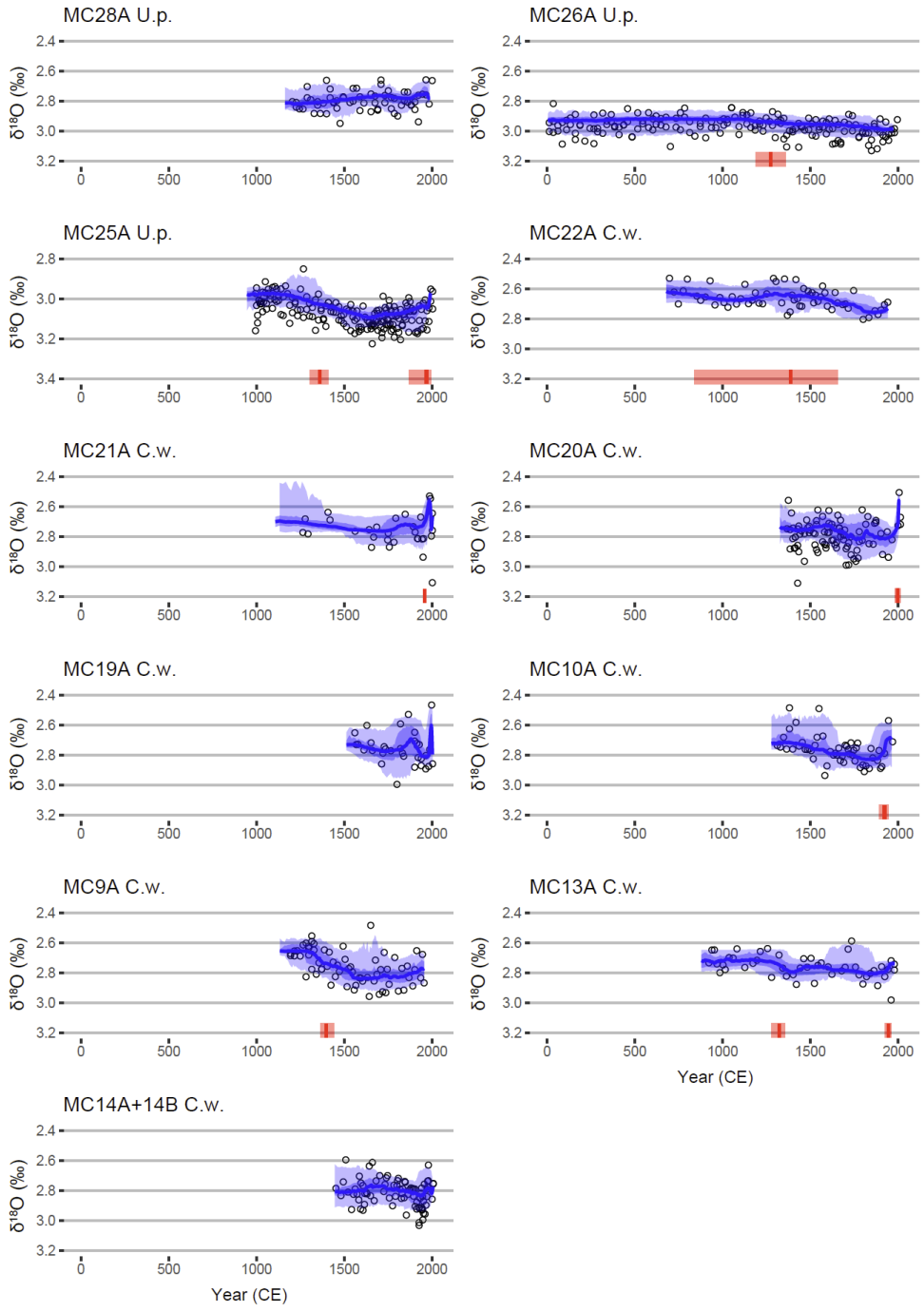

Fig. S6. Benthic $\delta^{18}O$ records of eleven EN539 multicores. The thick blue line shows the median ensemble member; dark and light blue show the 50% and 90% highest-density probability ranges, respectively; circles denote raw $\delta^{18}O$ data using median BACON age as x-axis. Red bars denote the ranges of change point in each record, with thick red lines marking the mean change point age. Five cores (MC26A, 25A, 22A, 9A, 13A) show significant $\delta^{18}O$ increases during MCA-LIA transitions; five cores (MC25A, 21A, 20A, 10A, 13A) show significant $\delta^{18}O$ decreases near the top. U.p.: *U. peregrina*; C.w.: *C. wuellerstorfi*.

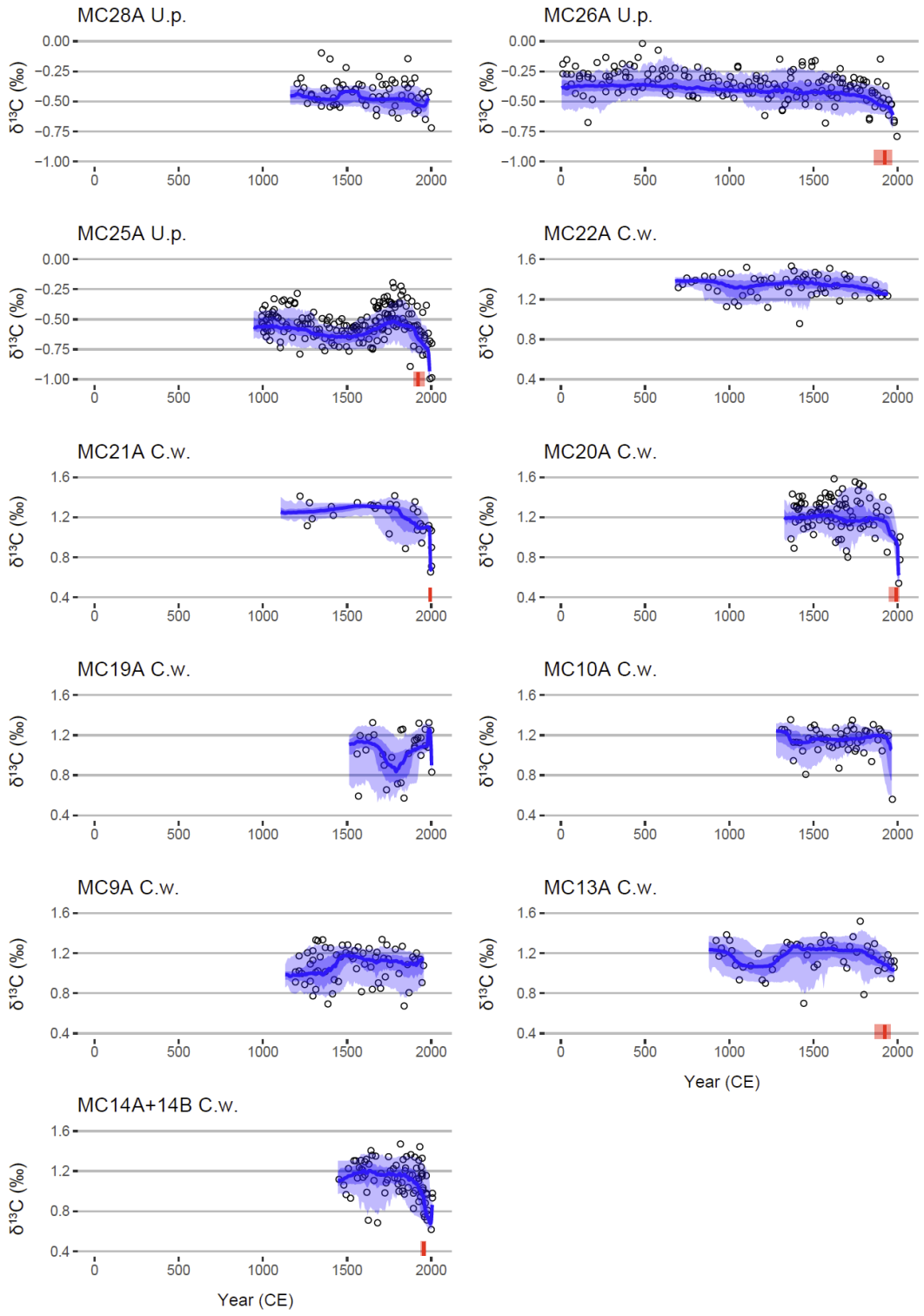

Fig. S7. Benthic $\delta^{13}C$ records of eleven EN539 multicores. Six cores (MC26A, 25A, 21A, 20A, 13A, 14A) show significant $\delta^{13}C$ decreases near the top. Red bars denote the ranges of change point in each record, with thick red lines marking the mean change point age.

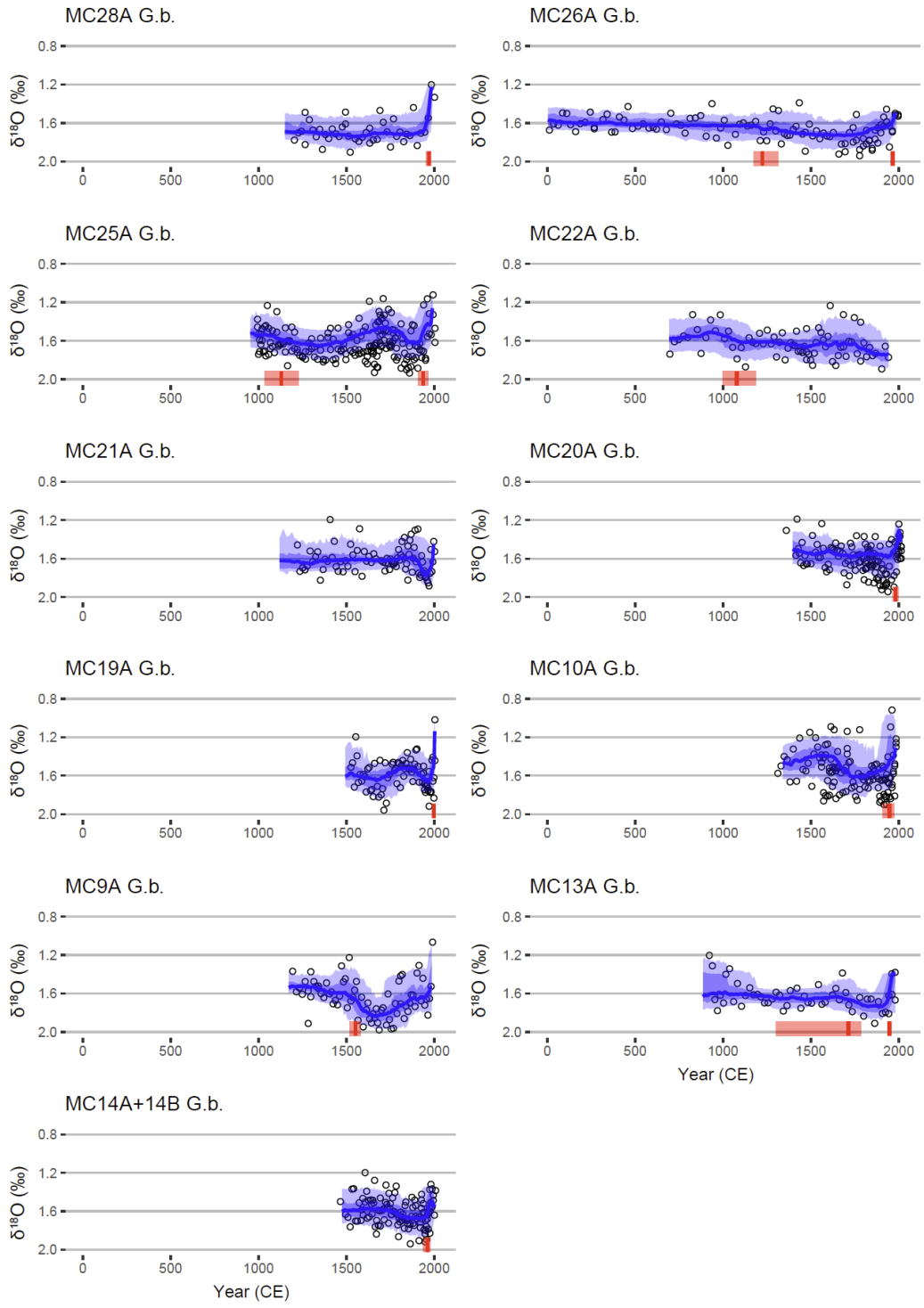

Fig. S8. *G. bulloides* $\delta^{18}O$ records of eleven EN539 multicores. Five cores (MC26A, 25A, 22A, 9A, 13A) show significant $\delta^{18}O$ increases during MCA-LIA transitions; all but three cores (MC22A, 21A, 9A) show significant $\delta^{18}O$ decreases near the top. Red bars denote the ranges of change point in each record, with thick red lines marking the mean change point age.

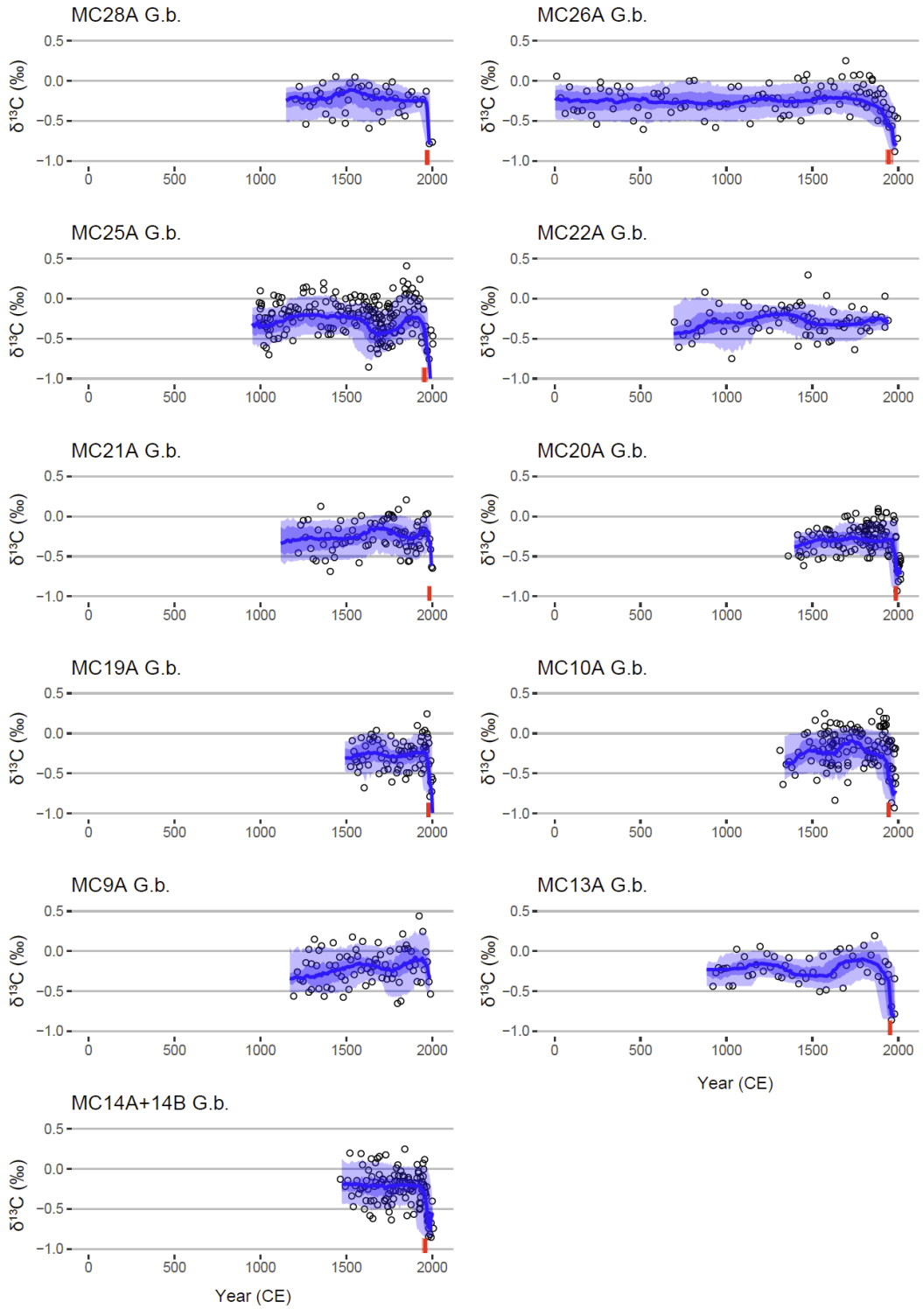

Fig. S9. *G. bulloides* $\delta^{13}C$ records of eleven EN539 multicores. All but two cores (MC22A and 9A) show significant $\delta^{13}C$ decreases near the top. Red bars denote the ranges of change point in each record, with thick red lines marking the mean change point age.

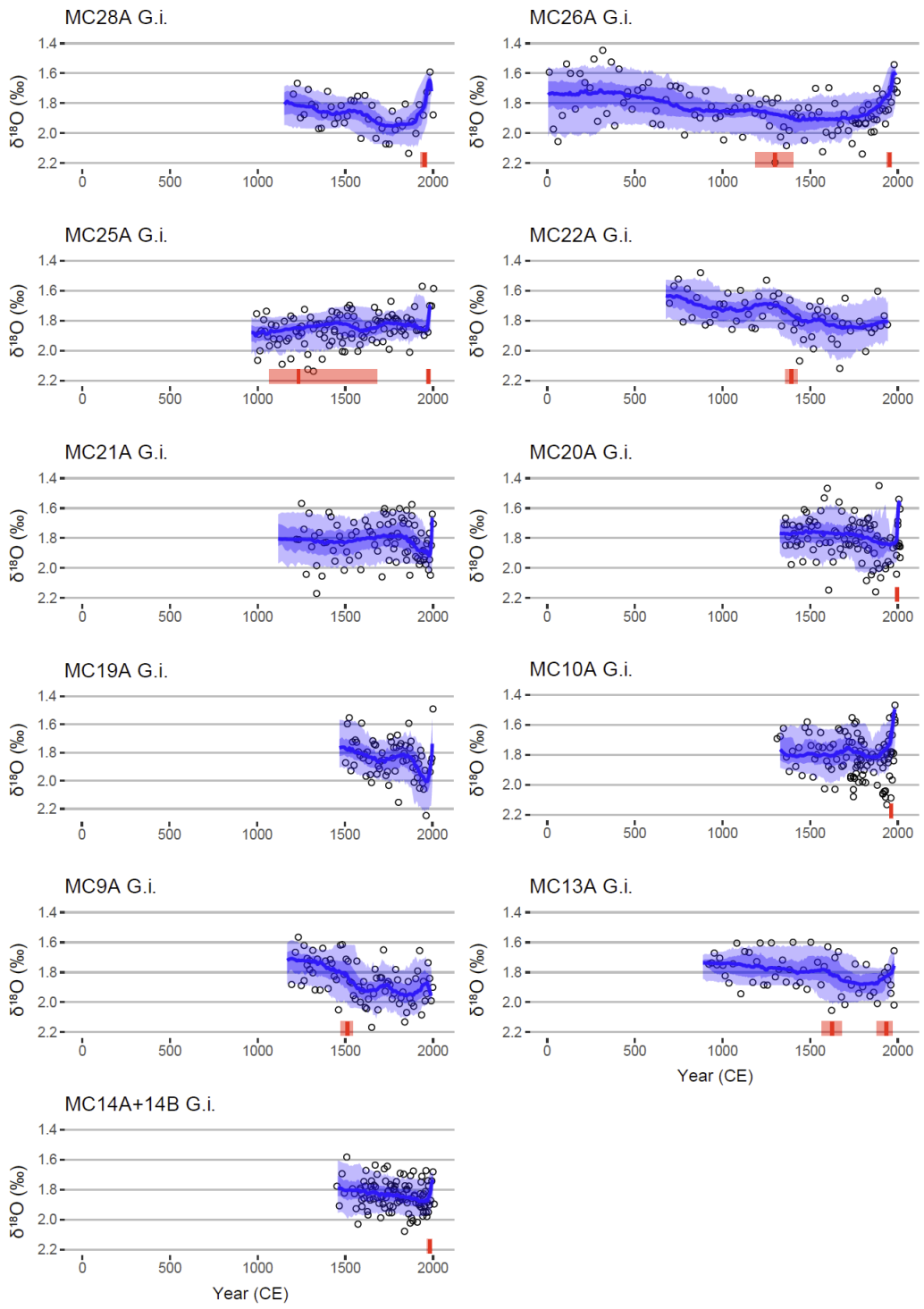

Fig. S10. *G. inflata* $\delta^{18}O$ records of eleven EN539 multicores. Five cores (MC26A, 25A, 22A, 9A, 13A) show significant $\delta^{18}O$ increases during MCA-LIA transitions; all but four cores (MC22A, 21A, 19A, 9A) show significant $\delta^{18}O$ decreases near the top. Red bars denote the ranges of change point in each record, with thick red lines marking the mean change point age.

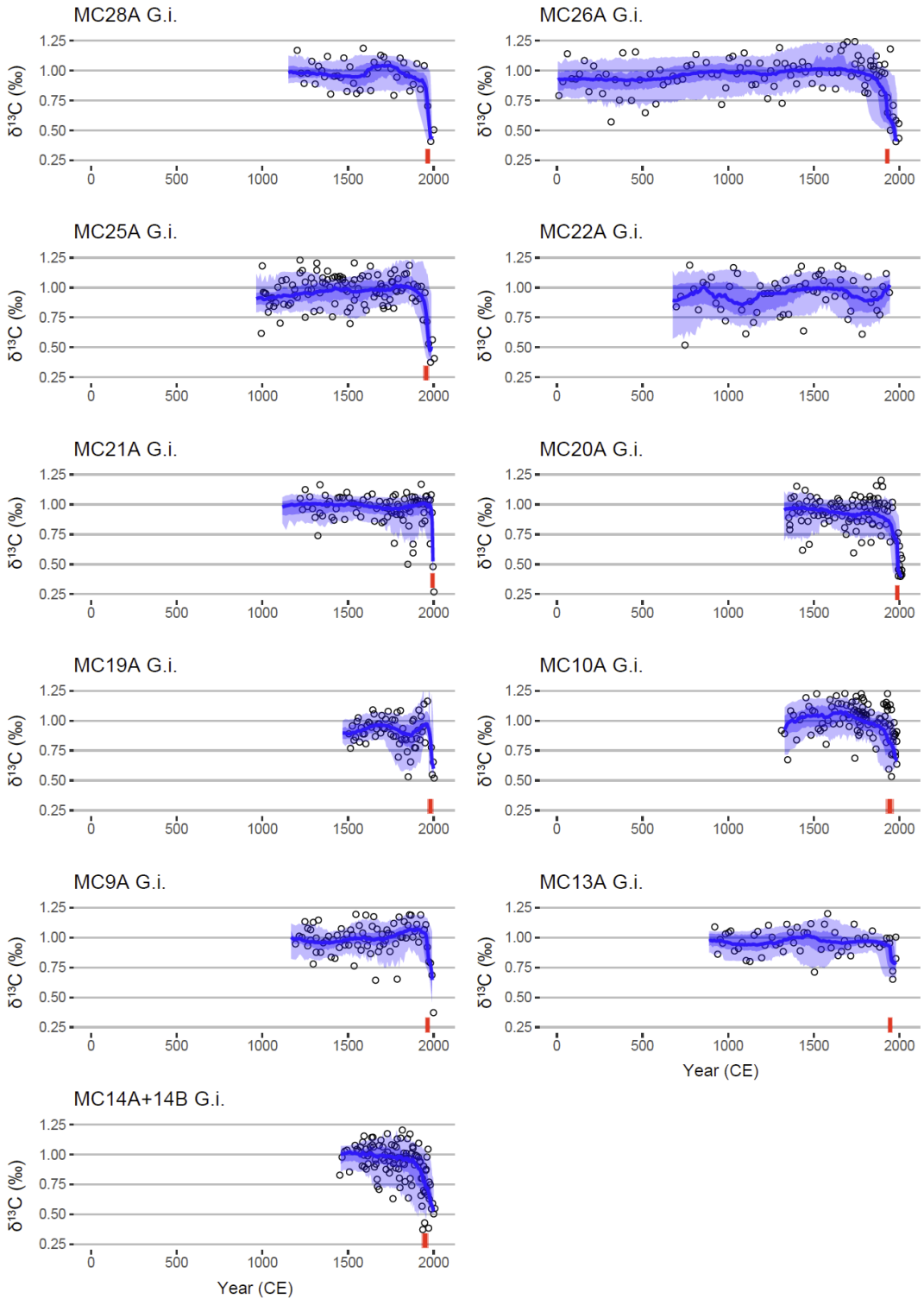

Fig. S11. *G. inflata* $\delta^{13}C$ records of eleven EN539 multicores. All but one core (MC22A, which does not have a modern top) shows significant $\delta^{13}C$ decreases near top. Red bars denote the ranges of change point in each record, with thick red lines marking the mean change point age.

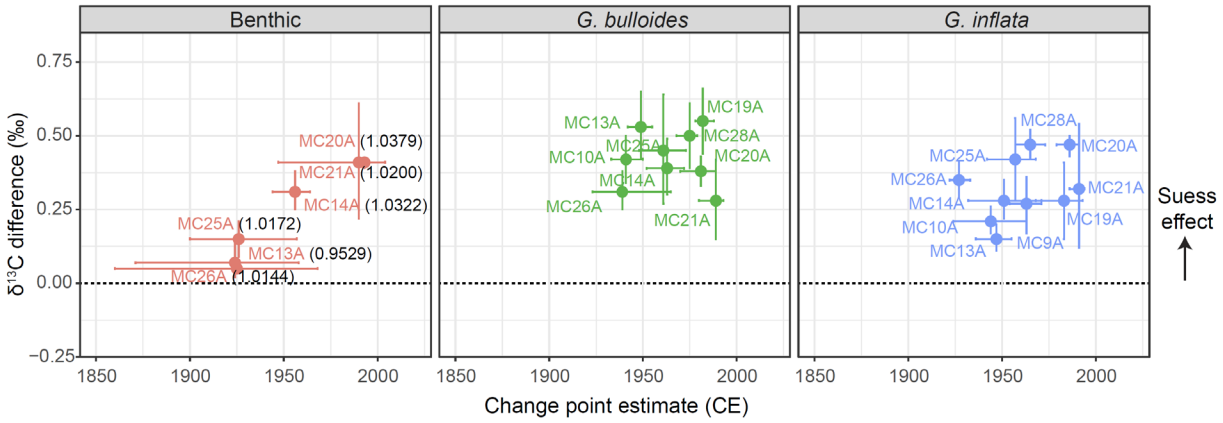

Fig. S12. Change point results of $\delta^{13}C$ records. The timing of significant $\delta^{13}C$ decrease near the top (Suess effect, (*17*)) in most cores is between 1925 and 2000 CE. Black numbers in the parentheses in the benthic figure denote ^{14}C Fm. Larger benthic $\delta^{13}C$ change are found in cores with younger core-top sample ages (higher Fm). The younger change point may occur because we assigned younger core-top ages to cores with higher Fm and/or because the benthic $\delta^{13}C$ decrease is recorded as a more abrupt change in these cores.

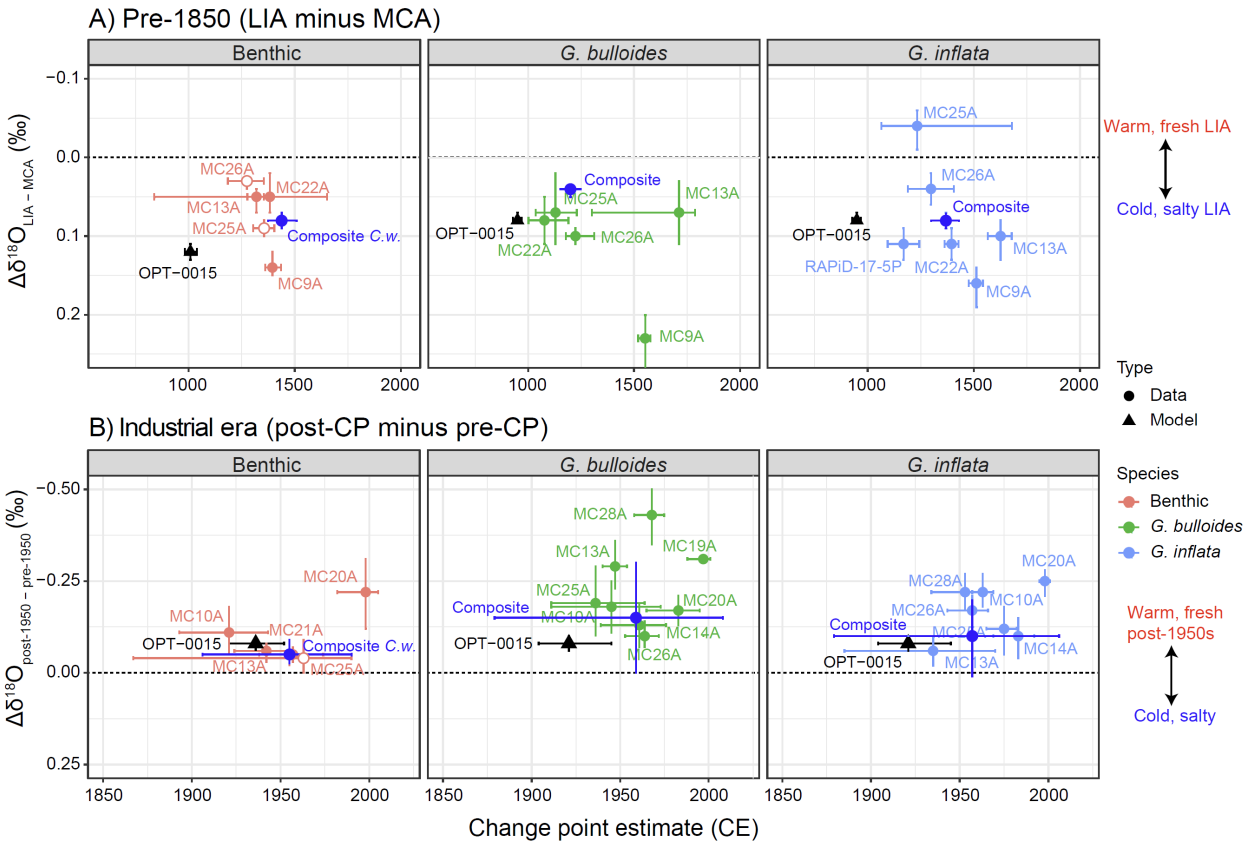

Fig. S13. Change point results of $\delta^{18}O$ records, same as Fig. 3 but zooming in to the post-1850 dataset to show change point distributions. Change points of the composite stacks (Fig. S14) are also shown.

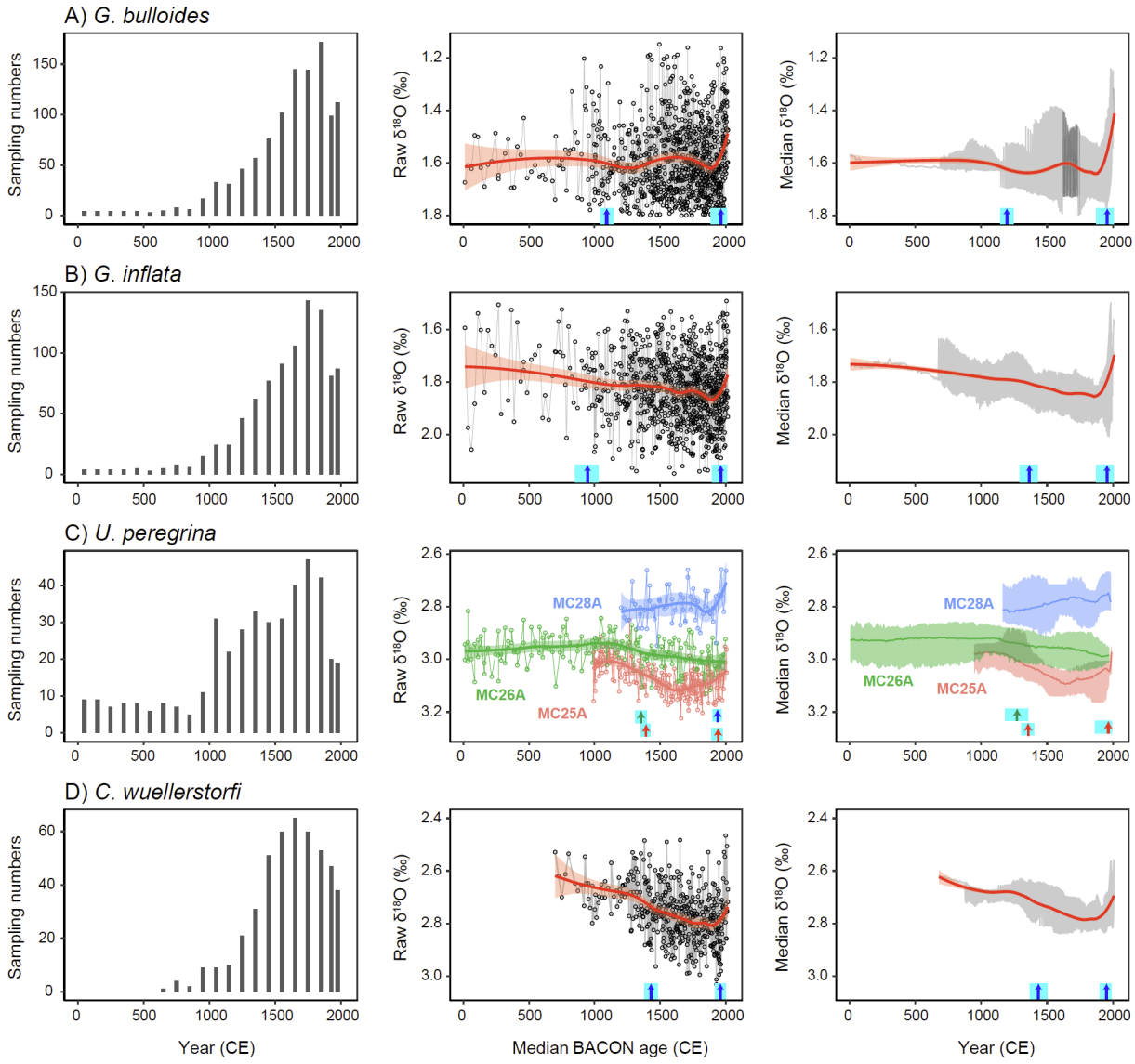

Fig. S14. Number of samples measured in every 100-year interval from 0 to 1900 and 50-year intervals from 1900 to 2010 (left panels), along with smoothed records of all raw $\delta^{18}O$ data on their median BACON ages (middle panels), and composites constructed of all records on their median $\delta^{18}O$ ensembles (right panels). The smoothing used a LOESS method (local polynomial regression fitting) from R software package "ggplot2". Note a composite *U. peregrina* record was not generated as the three records are distinctly different from each other. Cyan bars denote the ranges of change point in each composite record, with thick arrows marking the mean change point age. For the post-1850 dataset of site MC28A, although the median $\delta^{18}O$ ensemble did not pass the CP significance test (right panel), the smoothed raw $\delta^{18}O$ record passed the CP significance test and suggested warming/freshening at ~1941 CE (middle panel). The large noise in the planktic records, which is likely due to spatial variability and seasonal and depth habitat changes of planktic foraminifera, justifies our strategy of carrying out CP analysis on the individual records. The relatively early MCA-LIA CP in the smoothed planktic records (middle panels) compared to the individual records (Fig. 3, S13) and the

composite records of median $\delta^{18}O$ ensemble (right panels) likely arises because the early part of the records is from just one core (MC26A), and there is a dramatic increase in the number of data points before and after the CP. The benthic smoothed stack is less noisy, its CP falls where there are already data from several cores, and there is less of an increase in the number of data points before and after the CP, explaining why it is closer in time to the composite records of median $\delta^{18}O$ ensemble (right panels). The deepest *U. peregrina* record (MC25A; 1310 m) and the *C. wuellerstorfi* stack (1500 – 2300 m) suggest an increase of about ~0.1‰ from the MCA to the coldest temperatures of the LIA, equivalent to ~0.5°C cooling, similar to the estimates of the CPs from the individual records (Fig. 3A).

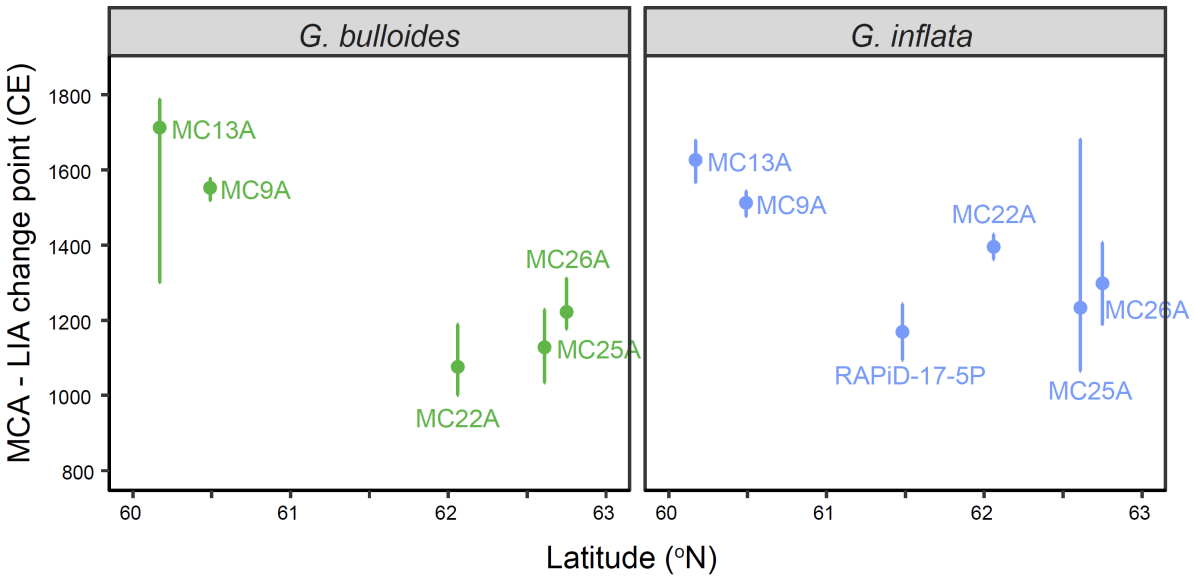

Fig. S15. Cross-plot of planktic MCA-LIA change point versus site latitude. Earlier LIA cooling at planktic records may imply earlier cooling at the northern than southern sites.

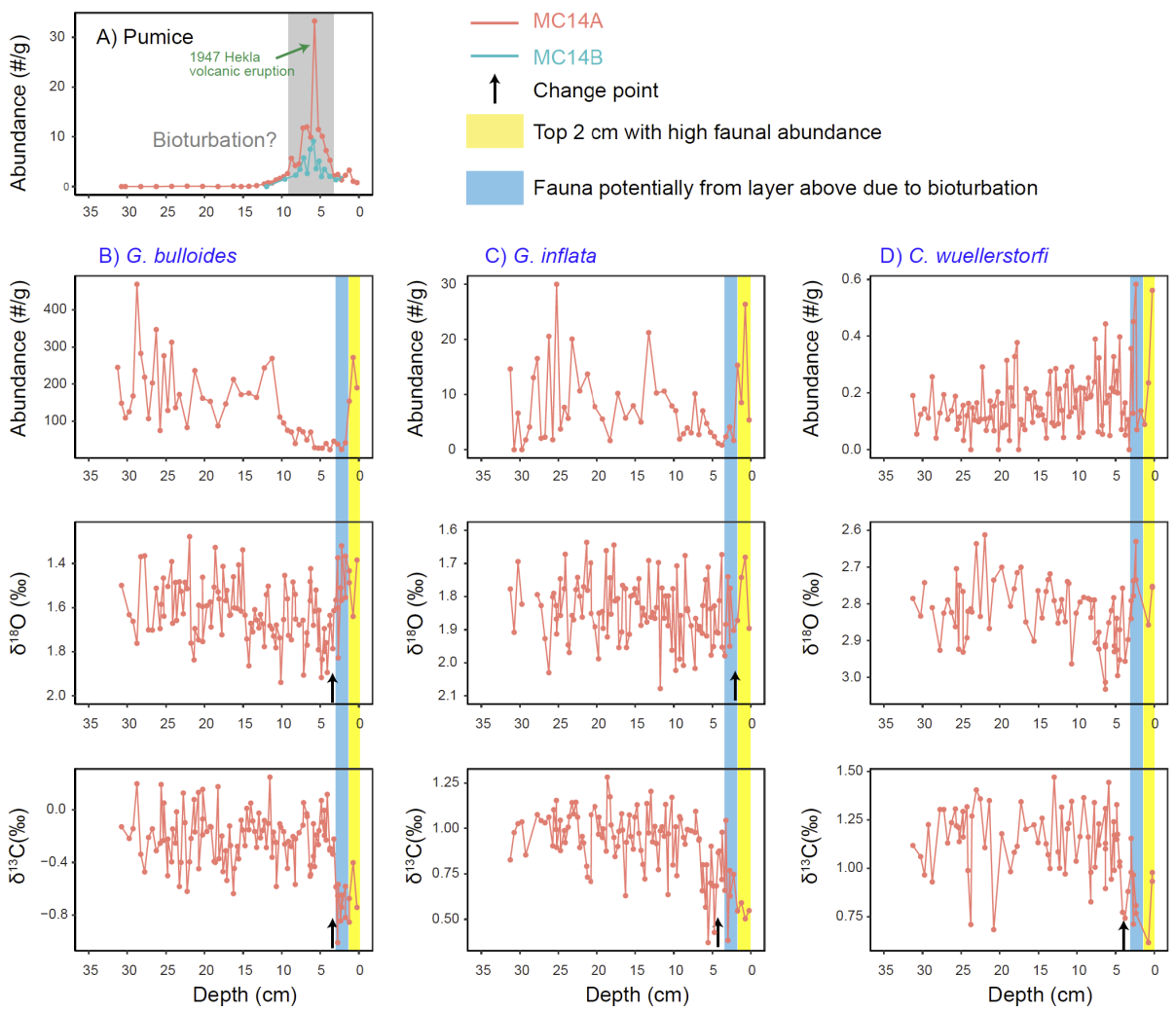

Fig. S16. Pumice (A), planktic (B-C), and benthic (D) foraminiferal abundance along with isotope records at site MC14 (combined A and B cores). If bioturbation occurred in the upper ~4 cm, the change points may have been more recent than suggested by our analyses.

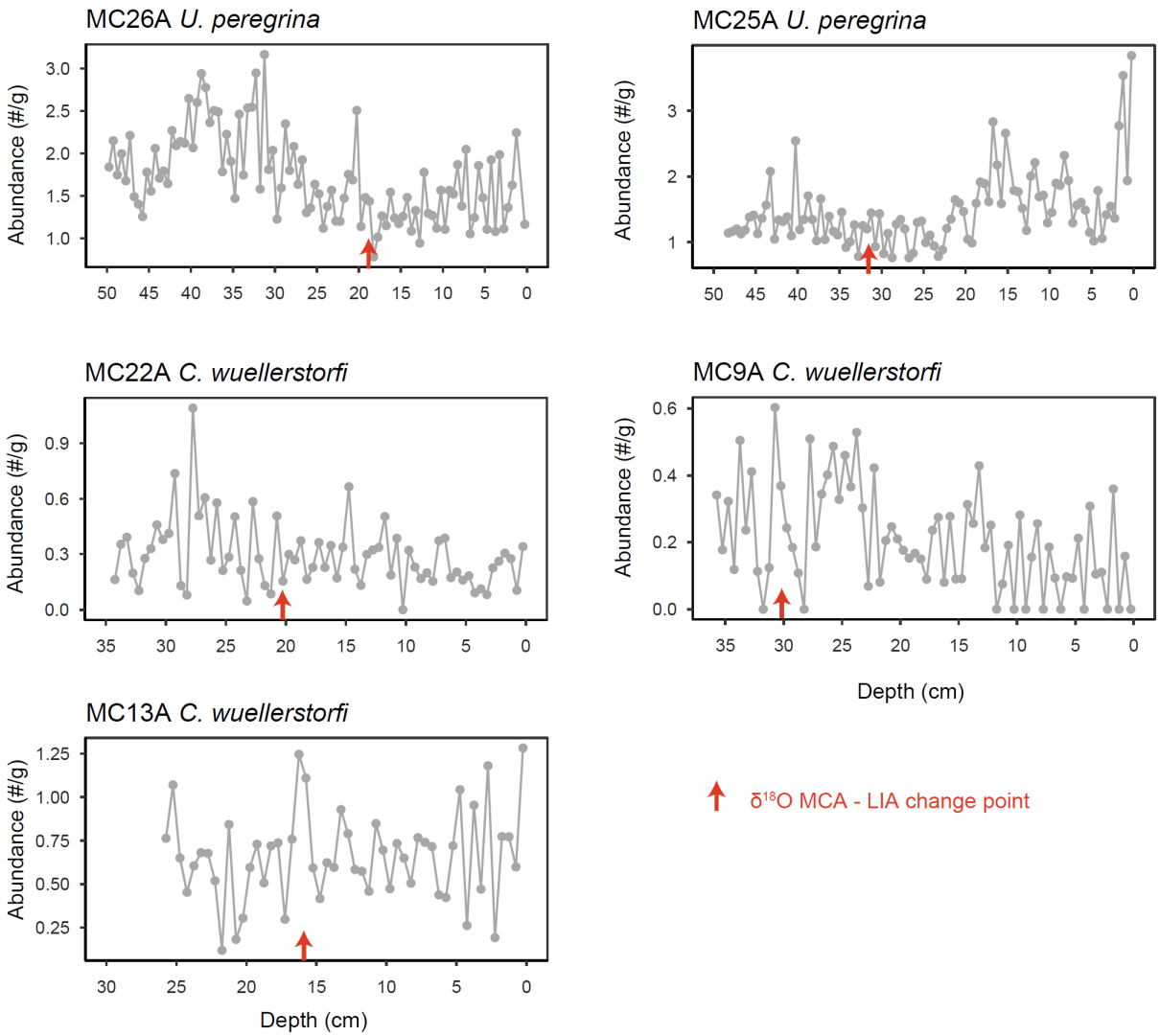

Fig. S17. Benthic abundance records in five sites which show significant $\delta^{18}O$ change across the MCA – LIA transition. No clear benthic abundance changes occur at depths that are identified to record MCA-LIA changes (also note that there are generally few specimen/grams of dry sediment). Thus bioturbation, if present, should have had limited impact on the MCA-LIA benthic change point results.

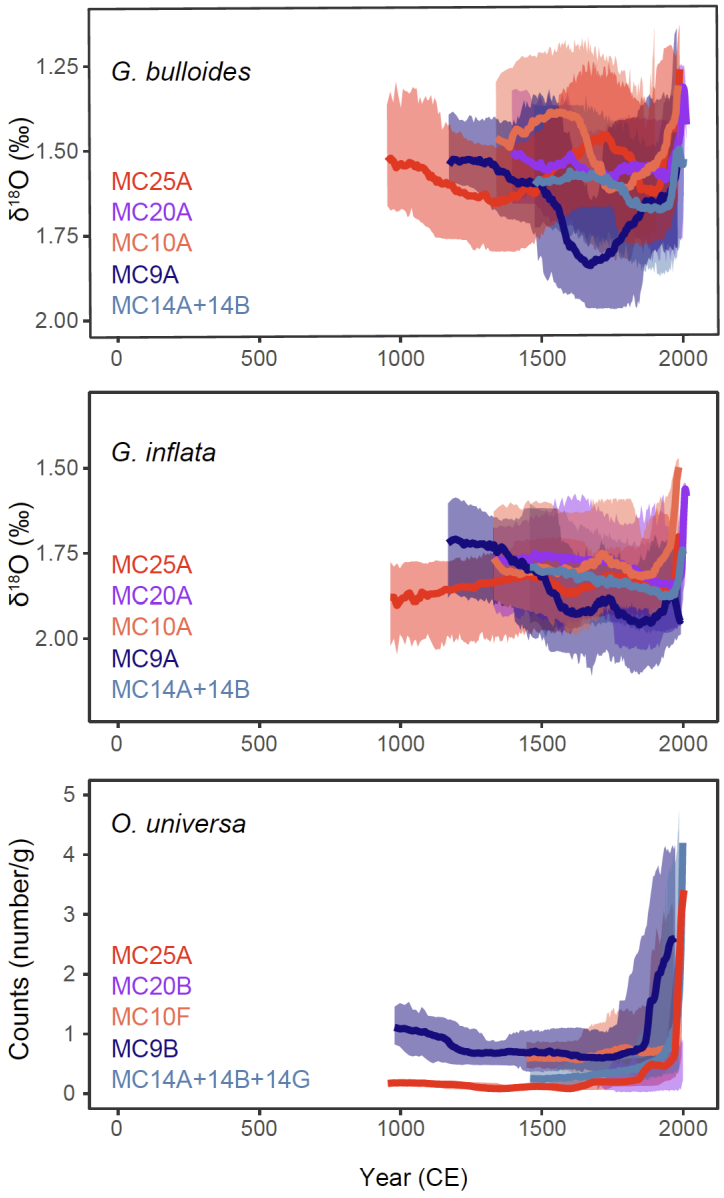

Fig. S18. Comparison of planktic $\delta^{18}O$ with abundance of warm-water species *Orbulina universa* in the same cores. The *O. universa* abundance records from MC25A, 20B, 14A, and 14B are from ref. (*20*), all other records are from this study. The rapid increase of *O. universa* near the core-tops indicates a response to the recent warming in the Iceland Basin, supporting our inference that $\delta^{18}O$ decreases since ~1950s at least in part reflect surface warming.

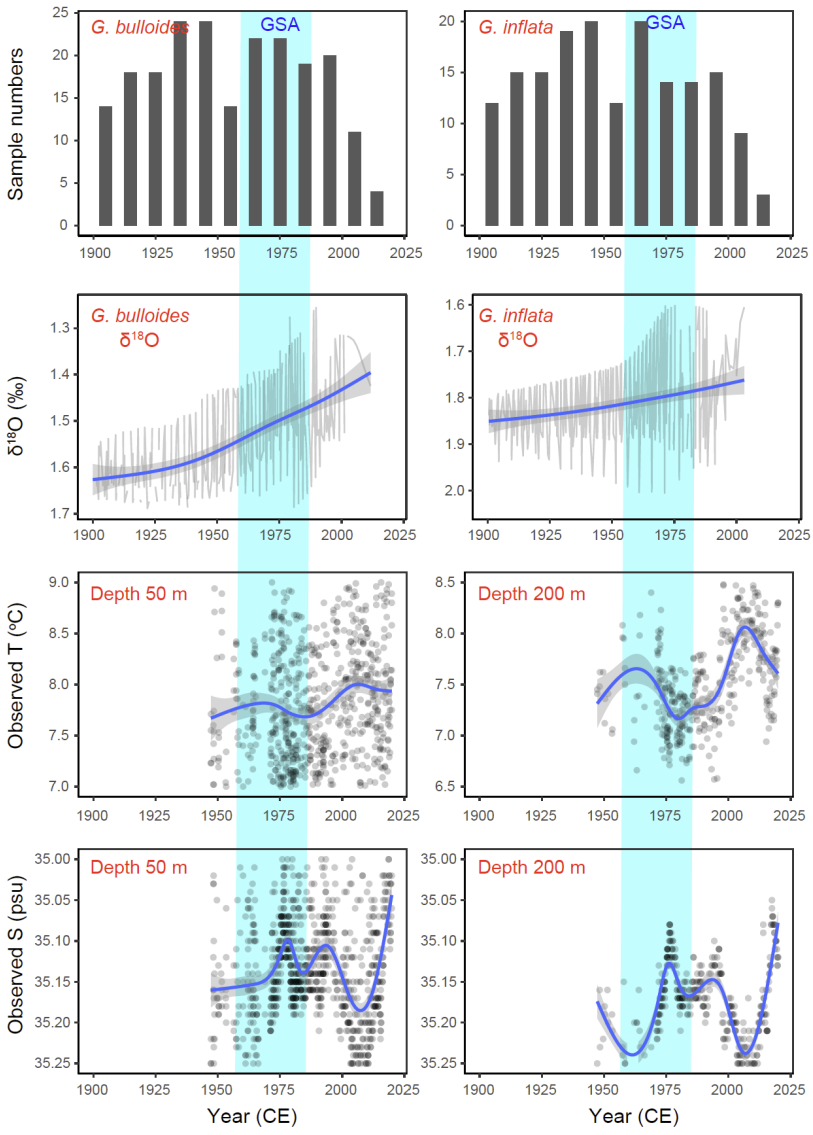

Fig. S19. Comparison of planktic $\delta^{18}O$ with instrumental temperature and salinity records stations south of Iceland near the core sites. Top row: number of planktic measurements in each bin, for *G. bulloides* (left) and *G. inflata* (right) from Fig. S14. Second row: smoothed $\delta^{18}O$ records of all median ensembles as in Fig. S14. Bottom two rows are observed temperature and salinity from water depths corresponding to the calcification depths of the planktic foraminifera. Note the salinity axis is reversed. The observational records were extracted from five Selvogsbanki stations, south of Iceland, with latitudes ranging from 63.0 to 63.41°N, and longitudes ranging from 20.41 to 21.28°W, from the Marine and Freshwater Research Institute, Iceland (https://sjora.hafro.is/). The light blue shading marks the "Great Salinity Anomaly" (GSA) from 1960s to 1990s, when the southward shift of the Polar Front allowed cold and fresh waters from Arctic Ocean to enter the northern North Atlantic Ocean (*48*). The overall warming and freshening trends since 1950 suggest that the recent decrease in planktic $\delta^{18}O$ likely reflects both warming and freshening.

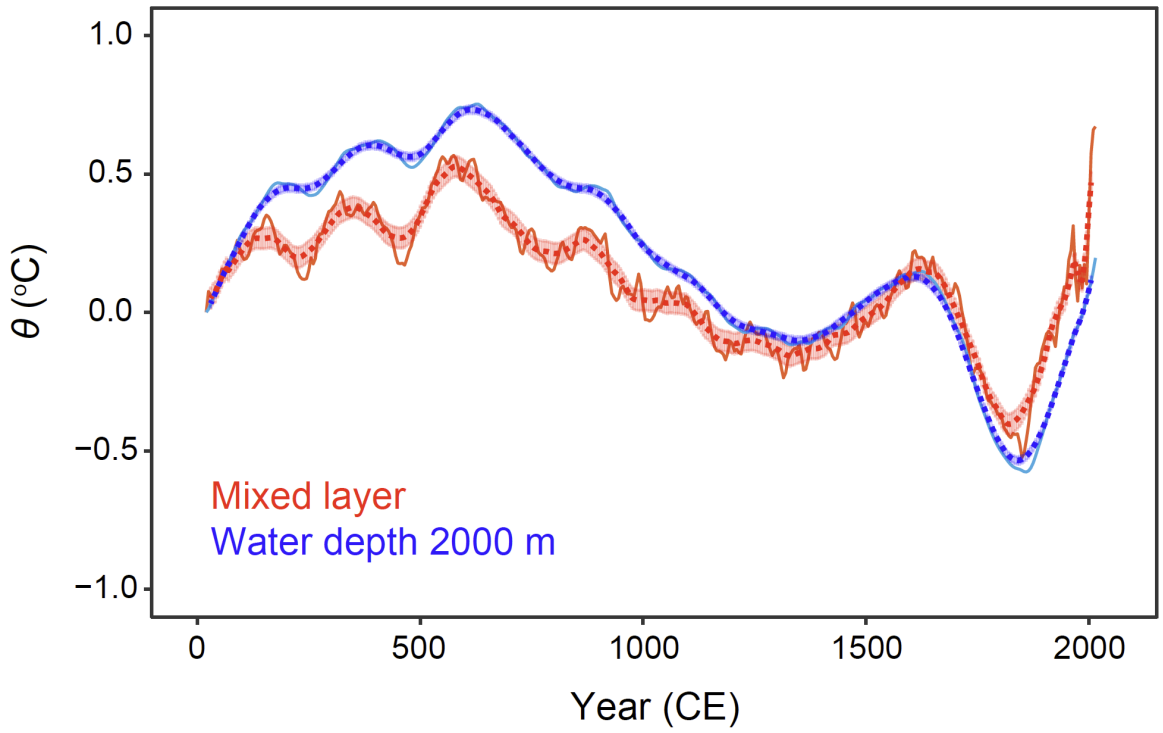

Fig. S20. Temperature evolution south of Iceland (a grid box of 61.5°N, 20.5°W) from the OPT-0015 inversion (*25*). The temperature evolution is identical in the upper 500 m (Fig. 4), thus we only plotted the results of mixed layer. The moving average (dashed lines) and error bars (shaded areas) were used as data input for change point analyses. Note that the moving averages were calculated on 20-yr moving window for the first and last 45 yrs. The error bars were calculated as the average difference of moving average curve and raw model output.

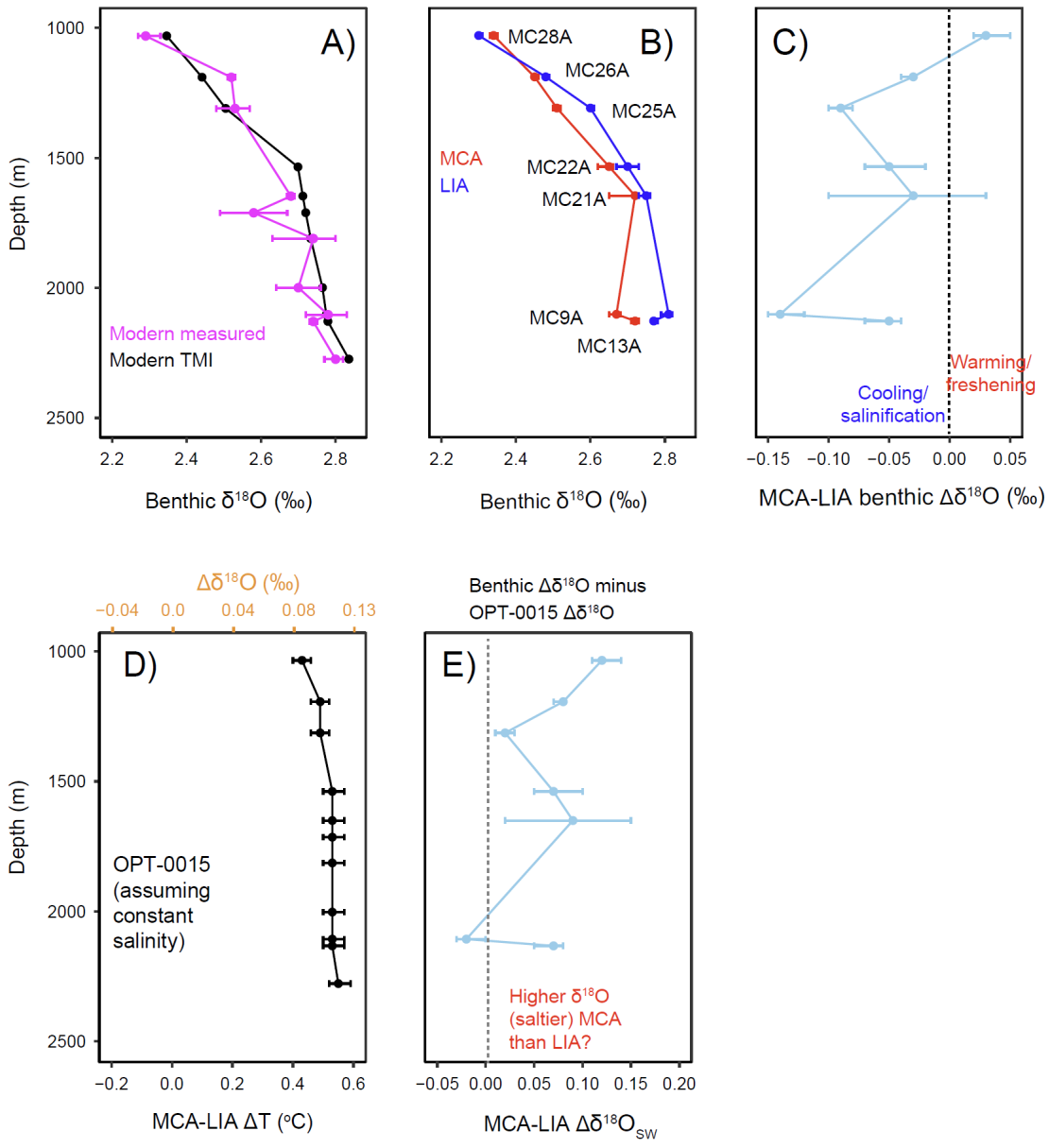

Fig. S21. Benthic $\delta^{18}O$ depth profiles in the modern and the MCA vs. LIA. The average benthic $\delta^{18}O$ values are from the change point results (Data S4), thus the modern profile includes samples with median ages between ~1920 and 2010; The MCA profile includes samples with ages older than ~1350; and LIA profile includes samples with ages between ~1350 and 1850. The OPT-0015 inversion assumes constant salinity and predicts 0.43 – 0.55 ˚C MCA-LIA cooling (D). If the MCA-LIA temperature changes from the OPT-0015 inversion are assumed accurate, the residual benthic $\delta^{18}O$ changes in all but one record (MC9A) suggest a decrease in $\delta^{18}O_{SW}$ (freshening) (E).

Table S1. Locations, top and bottom ages of eleven EN539 multicores in this study. "nbin" denotes number of bins over which to calculate intervals.

Core	Latitude (°N)	Longitude (°E)	Water depth (m)	Core total length (cm)	Core-top ^{14}C Fm	Core-top ^{14}C Fm err	Core-top $\delta^{13}C$	Core-top age assigned in Bacon input	BACON_Top age min (CE)	BACON_Top age max (CE)	BACON_Top age median (CE)	BACON_Bottom age min (CE)	BACON_Bottom age max (CE)	BACON_Bottom age median (CE)	Ave.acc. rate (cm/kyr)	Age span (yr)	nbin (5-yr interval) for geoChronR
EN539-MC28A	62.76	-20.67	1031	21	1.0081	0.0024	-0.97	1992	1958	1992	1983	991	1346	1198	27	785	157
EN539-MC26A	62.75	-20.68	1190	51	1.0144	0.0025	-0.80	1996	1972	1996	1988	-503	20	-246	23	2234	447
EN539-MC25A	62.61	-20.64	1310	50	1.0172	0.0022	-0.77	1998	1985	1998	1993	817	1160	1008	50	985	197
EN539-MC22A	62.06	-21.47	1535	35	0.9704	0.0028	-0.50	1970	1946	1970	1962	444	845	640	26	1322	264
EN539-MC21A	61.76	-21.67	1647	44	1.0200	0.0023	-0.99	1999	1992	2000	1996	928	1332	1124	50	872	174
EN539-MC20A	61.67	-21.73	1711	44	1.0379	0.0029	-0.94	2010	1999	2011	2006	1197	1470	1345	67	661	132
EN539-MC19A	61.42	-21.89	1810	36	1.0263	0.0033	-0.79	2003	1993	2004	2000	1351	1624	1489	69	511	102
EN539-MC10A	60.4	-23.64	1999	34	1.0009	0.0022	-0.50	1988	1977	1989	1984	1014	1369	1197	43	787	157
EN539-MC9A	60.49	-23.94	2103	37	1.0200	0.0024	-0.69	1999	1983	2000	1994	964	1308	1161	44	833	167
EN539-MC13A	60.17	-23.78	2129	27	0.9529	0.0021	-0.19	1988	1958	1988	1979	736	1088	936	26	1043	209
EN539-MC14A	61.35	-20.35	2274	32	1.0322	0.0023	-1.17	2007	1996	2008	2004	1228	1525	1385	51	619	124

Data S1. (separate file)

Data_S1.xlxs file contains radiocarbon ages for EN539 multicores.

Data S2. (separate file)

Data_S2.xlxs file contains age models for EN539 multicores plotted in Fig. S4.

Data S3. (separate file)

Data_S3.xlxs file contains raw isotope data and age-uncertain ribbon output from geoChronR plotted in Fig. 2 and S6-S11.

Data S4. (separate file)

Data_S4.xlxs file contains change point results shown in Fig. 3 and S12-13.